JGR Atmospheres

RESEARCH ARTICLE
10.1029/2019JD031582

Convectively Generated Gravity Waves During Solstice and Equinox Conditions

C. J. Heale[1], T. S. Lund[2], and D. C. Fritts[2]

[1]Center for Space and Atmospheric Research (CSAR), Embry-Riddle Aeronautical University, Daytona Beach, FL, USA, [2]GATS Inc, Boulder, CO, USA

Key Points:
- Strong winds and shears govern the morphology of concentric patterns
- Zonal mesospheric shears in solstice months lead to in situ breaking and further disruption of concentric patterns
- Weak winds and shears in equinox lead to more observable concentric patterns with breaking occurring in the lower thermosphere

Supporting Information:
- Supporting Information S1
- Movie S1
- Movie S2

Correspondence to:
C. Heale,
healec@erau.edu

Citation:
Heale, C. J., Lund, T., & Fritts, D. C. (2020). Convectively generated gravity waves during solstice and equinox conditions. *Journal of Geophysical Research: Atmospheres*, *125*, e2019JD031582. https://doi.org/10.1029/2019JD031582

Received 28 AUG 2019
Accepted 5 MAR 2020
Accepted article online 4 APR 2020

Author Contributions
Conceptualization: C. J. Heale, D. C. Fritts
Funding Acquisition: D. C. Fritts
Methodology: C. J. Heale, T. S. Lund
Software: T. S. Lund
Validation: T. S. Lund
Writing - Original Draft: C. J. Heale
Formal Analysis: C. J. Heale
Investigation: C. J. Heale
Project Administration: D. C. Fritts
Supervision: T. S. Lund, D. C. Fritts
Visualization: C. J. Heale
Writing - review & editing: C. J. Heale, T. S. Lund

Abstract Previous studies suggest that mesospheric concentric wave patterns are more observable in the equinox months than solstice months, despite concentric and semiconcentric waves being readily observed in summer months in the stratosphere. This study uses a 3-D nonlinear model to simulate the propagation and dissipation of convectively generated gravity waves under averaged equinox and solstice conditions to investigate the influences of wave breaking upon these concentric patterns. It is found that the relatively weak atmospheric winds and shears during the equinox months means that waves can propagate up to the lower thermosphere before breaking. In contrast, strong zonal winds and shears in the summer solstice months lead to in situ breaking in the mesosphere, which causes disruption to the concentric pattern. While the western propagating portion of the concentric pattern is filtered by the stratospheric winds, the eastern propagating portion rapidly transitions to turbulence in the mesosphere making it less likely to observe concentric patterns in the solstice months. The concentric pattern is more complete in the equinox months because the waves are only weakly filtered by winds and relatively little in situ breaking occurs in the mesosphere. However, in situ breaking does not affect the pattern in the stratosphere, where the morphology is primarily dictated by wind filtering. This also helps explain why concentric and semiconcentric patterns are observed in the summer stratosphere but not regularly in the mesosphere.

1. Introduction

Gravity waves are an important mechanism for transporting energy and momentum from the lower atmosphere to the middle and upper atmosphere (Fritts & Alexander, 2003). They are ubiquitous and play a crucial role in defining the structure and circulation of the Earth's atmosphere (e.g., Garcia & Solomon, 1985; Holton, 1982; Holton & Alexander, 2000; Lindzen, 1981). Gravity wave generation mechanisms include convection, flow over topography, and flow imbalances (e.g., Beres, 2004; Durran & Klemp, 1987; Lane et al., 2001; McFarlane, 1987; Nastrom & Fritts, 1992; Pfister et al., 1993; Richter et al., 2010; Song et al., 2003), and each generation mechanism produces a different source spectra and gravity wave propagation characteristics. Waves grow in amplitude as they propagate upward and can exhibit nonlinearity and wave breaking, leading to deposition of their energy and momentum into the mean flow (Fritts & Alexander, 2003; Holton, 1983; Holton & Alexander, 2000; Lindzen, 1981; Lund & Fritts, 2012; McFarlane, 1987) and secondary wave generation (Bossert et al., 2015; Holton & Alexander, 1999; Heale et al., 2017; Pandya & Alexander, 1999; Vadas et al., 2003, 2018). In addition, waves can be absorbed into the mean flow by critical level filtering if they encounter a wind equal to their own horizontal phase speed (Booker & Bretherton, 1967). If the waves propagate into the thermosphere without breaking, or being filtered, waves will be dissipated by increasing molecular viscosity and thermal conductivity (Heale et al., 2014, 2018; Hickey et al., 2011; Vadas, 2007; Vadas & Fritts, 2005). Gravity waves also couple to nonneutral modes in the upper atmosphere and are linked to phenomena such as traveling ionospheric disturbances (Burleigh et al., 2018; Hocke & Schlegel, 1996; Hunsucker, 1982; Kirchengast et al., 1995).

Gravity waves generated by convection are particularly important in the summer hemisphere tropical and midlatitudes (Gong et al., 2015; Hoffmann & Alexander, 2010; Perwitasari et al., 2016; Tsuda et al., 2000). Gravity waves generated by convection in the troposphere help in initiating and organizing further tropical convection (Lane & Moncrieff, 2008; Mapes, 1993) and can contribute to clear air turbulence that can affect aircraft (Lane & Sharman, 2008). In the stratosphere, convectively generated waves contribute to the driving of the Quasi-Biennial Oscillation (Alexander & Holton, 1997; Piani et al., 2000), the Semi-Annual Oscillation

(Ern et al., 2015; Garcia et al., 1997), and Brewer-Dobson Circulation (Alexander & Rosenlof, 2003; Stephan et al., 2016). In the mesosphere and lower thermosphere, gravity waves can produce localized forcing and heating/cooling through dissipation by molecular viscosity and thermal conduction (Hickey et al., 2011; Vadas & Fritts, 2005) and also undergo strong nonlinearity and breaking that generates secondary waves (Heale et al., 2017; Horinouchi et al., 2002; Vincent et al., 2013).

Numerous numerical studies have been performed to understand the mechanisms within convection that generate gravity waves (Lane et al., 2001; Pandya & Alexander, 1999; Song et al., 2003). The three main mechanisms put forward are (1) diabatic heating, (2) the mechanical oscillator (Fovell et al., 1992), and (3) the obstacle/moving mountain effect (Pfister et al., 1993). The first represents the latent heating associated with precipitation within a convective system. The second represents the body forcing associated with overshoot into the stable stratosphere from the tropopause, and the third represents the notion of ambient flow having to redirect around the convective system, which acts as an obstacle. A review of these mechanisms and the coupling between them is presented in Song et al. (2003). It is suggested that the effective nonlinear forcing terms (arising from momentum and heat flux divergences) act out of phase to the diabatic heating, thus the inclusion of one without the other can overestimate the amplitudes of the waves by 2–3 times. However, the interaction with the background atmospheric wind and temperature structures plays a crucial role in the shape of the spectrum and filtering can affect the ability of waves to reach the stratosphere and beyond (Alexander & Holton, 2004; Beres et al., 2002; Song et al., 2003; Walterscheid et al., 2001; Vadas et al., 2009).

Theoretical and numerical studies have also been widely used to identify the typical spectra of waves that come from convective sources (Alexander & Holton, 1997; Beres et al., 2004; Choi & Chun, 2011; Fovell et al., 1992; Holton & Alexander, 1999; Lane & Sharman, 2008; Lane & Moncrieff, 2008; Lane et al., 2001; Piani et al., 2000; Song et al., 2003). Convection produces a broad spectra of waves with horizontal scales ranging from tens to hundreds of kilometers and periods ranging from minutes to hours. Single-cloud systems have been shown to generate the strongest wave power at horizontal wavelengths between 5–50 km and 10–60 min periods (Lane & Moncrieff, 2008). The wave modes generated are related to the temporal and spatial scales of individual plumes up to the scales of the whole thunderstorm system. Tropical multiscale convection, such as oceanic tropical convection, can produce flat momentum flux spectra with 10–1,000 km horizontal scales, but these are typically more benign than strong MCS and squall lines, for example (Lane & Moncrieff, 2008).

Gravity waves generated by thunderstorm systems can produce concentric or semi concentric patterns that are easily identifiable in satellite or ground-based imagery (Azeem et al., 2015; Gong et al., 2015; Hoffmann & Alexander, 2010; Miller et al., 2015; Perwitasari et al., 2016; Randall et al., 2017; Sentman et al., 2003; Suzuki et al., 2007; Wen et al., 2018; Xu et al., 2015; Yue et al., 2009, 2014). This provides an excellent method of assessing the scales and intensity of waves generated by convection. However, satellite observations also suffer from observational filtering of certain horizontal wavelength and vertical wavelength ranges and ground-based instruments suffer from a small field of view. In addition, both ground and space based observations are typically limited to a single layer. Certain instruments are also biased toward detecting waves of certain scales that can skew statistics about the spectra of waves in the atmosphere (Kalisch et al., 2016; Trinh et al., 2016). Therefore, comprehensive studies of the convective gravity wave life cycle require multilayer, multi-instrument observations and numerical modeling to study the evolution and coupling of these waves.

Perwitasari et al. (2016) and Gong et al. (2015) performed global studies of concentric gravity waves (CGWs) in the mesosphere and stratosphere respectively. Gong et al. (2015) studied concentric rings in the Atmosphere Infrared Sounder (AIRS) radiance data during January and July 2010. They found that CGWs are mostly associated with tropical and subtropical deep convection in summer and extratropical jet imbalance, fronts, and convection in winter. Perwitasari et al. (2016) studied 3 years of CGWs at the mesopause using the IMAP/VISI instrument onboard the International Space Station. They found that the latitudinal distribution had peaks at midlatitudes (40°N and 40°S) and a minimum at low latitudes (10°S). Notably, the CGW occurrence rate switched between the Northern and Southern Hemispheres around the equinoxes and the occurrence probability was significantly higher during nonsolstice months than solstice months. In contrast to Gong et al. (2015), Perwitasari et al. (2016) found very few CGW events over the tropical convective regions.

Vadas et al. (2009) studied the effects of equinox and solstice wind profiles on observed mesospheric concentric wave patterns using ray tracing in the linear limit. They found that strong winds (such as those in solstice conditions) produce distorted arc-like patterns rather than concentric patterns. In addition, the strong winds can act to critical level filter and reflect certain wave modes before they reach the mesosphere thus removing them from the concentric pattern. It was also noted that the winds can shift the apparent center of the concentric ring from the plume location as viewed at 87 km. For concentric patterns to form, the wind amplitude and variation below the altitude of interest should be small (such is the case in equinox conditions).

In this paper, we investigate the effect of solstice and equinox wind and temperature conditions on concentric patterns generated by convectively generated gravity waves in the nonlinear limit. We use the Complex Geometry Compressible Atmosphere Model to launch gravity waves from a single convective plume source in monthly averaged March, July, and September conditions. In particular, we investigate the morphology, directionality, spectrum, amplitude, and nonlinearity of the wave patterns in the stratosphere and mesosphere as these are commonly observed regions by satellite imagery. The primary difference between this paper and previous works such as Vadas et al. (2009) is the inclusion of nonlinearity and wave breaking and consideration of the affect these have on the concentric morphology. The paper is organized as follows: section 2 describes the model and simulation setup, section 3 describes the results and analysis, and section 4 provides a summary and conclusions.

2. Numerical Model and Simulation Setup

2.1. Numerical Model

The numerical model used for the simulations in this paper is the Complex Geometry Compressible Atmosphere Model (Felten & Lund, 2006). We start with the compressible Navier-Stokes equations, written in strong conservation law (divergence) form

$$\frac{\partial \rho}{\partial t} + \frac{\partial \rho u_j}{\partial x_j} = 0, \tag{1}$$

$$\frac{\partial \rho u_i}{\partial t} + \frac{\partial \rho u_i u_j}{\partial x_j} = -\frac{\partial p}{\partial x_i} - \rho g \delta_{i3} + \frac{\partial \sigma_{ij}}{\partial x_j}, \tag{2}$$

$$\frac{\partial \rho E}{\partial t} + \frac{\partial (\rho E + p) u_j}{\partial x_j} = -\rho g u_3 + \frac{\partial u_i \sigma_{ij}}{\partial x_j} - \frac{\partial q_j}{\partial x_j}, \tag{3}$$

where σ_{ij} and q_j are the viscous stress and thermal conduction, defined as

$$\sigma_{ij} = \mu \left[\left(\frac{\partial u_i}{\partial x_j} + \frac{\partial u_j}{\partial x_i} \right) - \frac{2}{3} \left(\frac{\partial u_k}{\partial x_k} \right) \delta_{ij} \right], \tag{4}$$

$$q_j = -k \frac{\partial T}{\partial x_j}, \tag{5}$$

and where μ is the dynamic viscosity, k is the thermal conductivity, δ_{ij} is the Kronecker delta, and g is the gravitational acceleration.

The solution variables are the density, ρ, the momentum per unit volume ρu_i, and the total energy per unit volume $\rho E = \rho(e + 1/2 u_k u_k)$, where $e = c_v T$ is the internal energy per unit mass. Here c_v is the heat capacity at constant volume and T is the temperature. The pressure p appears as an auxiliary variable and it is related to the density and temperature through the ideal gas law

$$p = \rho R T, \tag{6}$$

where R is the gas constant.

The governing equations are discretized using the finite volume framework, in which each computational cell is considered to be a small control volume. The solution variables are stored at the cell centroids and

fluxes on the faces are constructed using a kinetic energy-conserving scheme similar to that discussed in Felten and Lund (2006). The resulting scheme is globally conservative for mass, momentum, total energy, and kinetic energy. Time advancement is achieved via a low-storage, third-order accurate Runge-Kutta scheme.

In order to enhance numerical stability, most common schemes contain some form of numerical dissipation. While this achieves its purpose, it violates kinetic energy conservation and can produce significant nonphysical damping of small-scale instability and turbulent structures. Our scheme, on the other hand, is stabilized via its kinetic energy-conserving construction and is therefore well suited for instability, transition, and turbulent flow regimes.

2.2. Domain and Convective Forcing

The domain used in this simulation is 1,000 km × 1,000 km × 200 km (x, y, and z) with resolutions of 1 km × 1 km × 0.5 km, respectively. The time step is ~0.3 s and the simulation is run for 3 hr with outputs ~30 s. The side and top boundaries are open and a 20 km wide sponge layer is applied to each. The bottom boundary is reflective.

The convective forcing is modeled as a latent heating applied to the energy term of the Navier-Stokes equations. The heating represents a single convective plume and parameters are based on estimates from previous studies (e.g., Alexander & Holton, 2004; Stephan & Alexander, 2015). The heating is ramped up and down over a 20 min period, the horizontal distribution of the heating follows a Gaussian with a half-width of 8 km, and the vertical distribution follows two half cosine waves (one representing the heating and the other representing the cold pool) based upon the algorithms of Stephan and Alexander (2015). The forcing is described in the equation below:

$$Q(x, y, z, t) = Q(z, t)exp(-0.5(x^2/\sigma_x^2 - y^2/\sigma_y^2)) \tag{7}$$

where

$$Q(z,t) = \begin{cases} Q(t)w_{heat}\cos\left(\frac{2\pi}{z_w}(z - z_c)\right), & \text{if } 1.75 \text{ km} < z < 11.25 \text{ km} \\ Q(t)w_{cool}\cos\left(\frac{2\pi}{z_{wl}}(z - z_{cl})\right), & \text{if } 0.25 < z < 1.75 \text{ km} \end{cases} \tag{8}$$

and

$$Q(t) = \begin{cases} 0.5(1 - \cos(\omega t)), & \text{if } 0 < t < 20 \text{ min} \\ 0, & \text{if } t > 20 \text{ min} \end{cases} \tag{9}$$

where $\sigma_x = \sigma_y = 8$ km, $w_{heat} = 0.025$ K/s, $w_{cool} = -0.0053$ K/s, $z_w = 19$ km, $z_{wl} = 3$ km, $z_c = 6.5$ km, $z_{cl} = 1$ km, and $\omega = \frac{2\pi}{20}$ min. Figure 1 shows the individual components of the forcing.

2.3. Atmospheric Profiles

The atmospheric background profiles are defined using NRLMSISE00 (Picone et al., 2002) for the temperature and density and HWM07 (Drob et al., 2008) for the zonal and meridional winds over Florida. The monthly averaged state was calculated for March, September (vernal and autumnal equinox states), and July (summer solstice state). Figure 2 shows the zonal winds as a function of day of year. The zonal winds tend to minimize around the equinoxes and maximize around the solstice. The dominant winds also change direction from eastward to westward about the equinoxes. Since winds play an important role in the filtering of CGWs in the atmosphere, the change in dominant wind direction will also change the propagation direction of the CGWs around the equinoxes.

The monthly averaged profiles for March, July, and September are displayed in Figure 3. The tropopause zonal wind shear and amplitude in March is much larger than in July and September. Studies show that the tropopause shear can have a significant influence on shaping the source spectrum of CGWs that propagate up into the stratosphere (Beres et al., 2002; Vadas et al., 2009); thus, we would expect the March tropopause wind to create a significantly asymmetric CGW spectrum in the lower atmosphere as compared to July and September. In July, the zonal wind is entirely in the westward direction above the tropopause and below 80 km and maximizes around the stratopause. The March zonal wind, in contrast, is entirely eastward below 80km but with smaller amplitudes and shears than in July. The zonal winds in September are smaller in magnitude than both the July and March cases and oscillate between eastward and westward. In the mesosphere and lower thermosphere region, there are considerable shears in the zonal wind in July

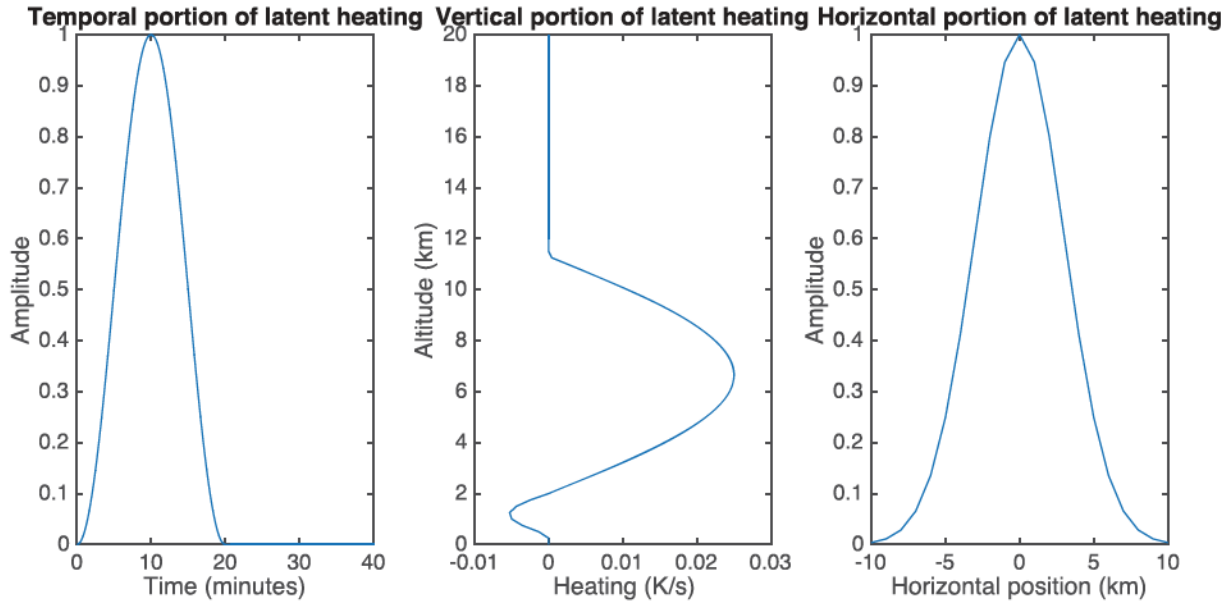

Figure 1. The temporal (left), vertical (middle), and horizontal (right) portions of the latent heating term added to the simulation to generate convection.

and September, but much smaller amplitude winds and shears in March. In general, the meridional winds are smaller and unimportant below the mesosphere and becomes appreciable (>10 m/s) only in the lower Thermosphere. Overall, considerably more critical level filtering and reflection of CGWs would be expected in the month of July than March or September.

3. Results and Analysis

The following section describes the results of the three case studies. In particular, results are presented in terms of an altitude slice at $z = 42$ km and $z = 85$ km. These correspond to the approximate altitudes that the AIRS satellite and OH imager would observe respectively. Vertical cross sections of the domain are also presented for $x = 0$, and $y = 0$ (middle of the domain), and the evolution is presented in terms of the vertical velocity perturbation (w'). It is noted that the aspect ratio of the zonal and meridional cross sections in

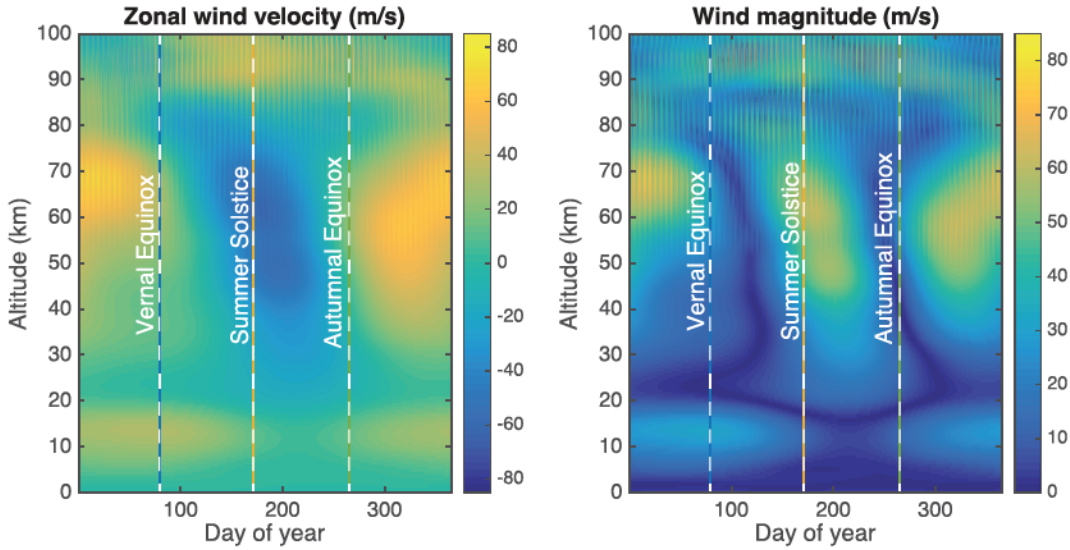

Figure 2. The zonal wind (left) and magnitude (right) as a function of day of year. Wind magnitudes are largest and most variable around the solstices and weakest around the equinoxes. The direction of the zonal wind in the upper stratosphere/mesosphere changes about the equinoxes.

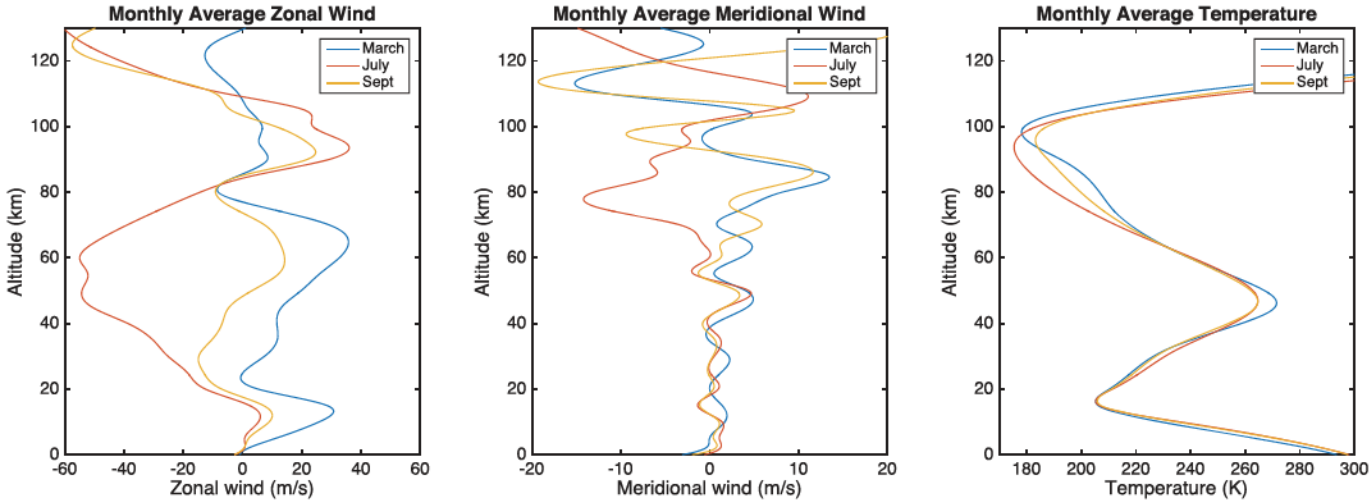

Figure 3. Monthly averaged zonal winds (left), meridional winds (middle), and temperatures (right) for March, July, and September. These profiles are used as background atmospheres for the three case studies in this paper.

Figures 5, 7, and 8 are distorted 10:1 to fit within the frame of the figures. Figure 4 shows an example of the zonal cross sections in each of the cases at $t = 2.1$ hr in the correct aspect ratio for reference. This highlights that the instabilities, which could be mistaken for steep phase lines, or numerical artifacts in the 10:1 aspect ratio, are in fact turbulent eddies occurring where the phase of the CGWs are refracted to small vertical scales. Video files showing the evolution of the fields described can be found in the supporting information.

3.1. Evolution and Morphology

3.1.1. March Evolution

The evolution of the CGW propagating through the March averaged background is shown in Figure 5. At 42 km altitude (top row in Figure 5), the CGW shows expanding concentric rings that decrease in amplitude as time progresses (from left to right). The amplitude is slightly greater for CGWs propagating westward (opposing the eastward winds at this altitude) and smaller scales are visible on the inner westward side of the ring as opposed to the eastward side. CGWs propagating against the wind will have larger vertical wavelengths and group velocities which enhances the vertical velocity perturbation. At $t = 2.6118$ hr (top right), smaller scales are seen embedded within the southward propagating portion of the concentric ring. These are the result of both downward propagating secondary waves generated by CGW breaking in the upper atmosphere and reflected waves. The secondary waves are generated by nonlinear processes associated with the CGW breaking and typically produce waves that are smaller than the primary breaking wave (e.g., Bossert et al., 2017; Chun & Kim, 2008; Heale et al., 2017; Satomura & Sato, 1999; Zhou et al., 2002; Snively & Pasko, 2008). This mechanism is different from the body forcing mechanism which generates secondary waves with

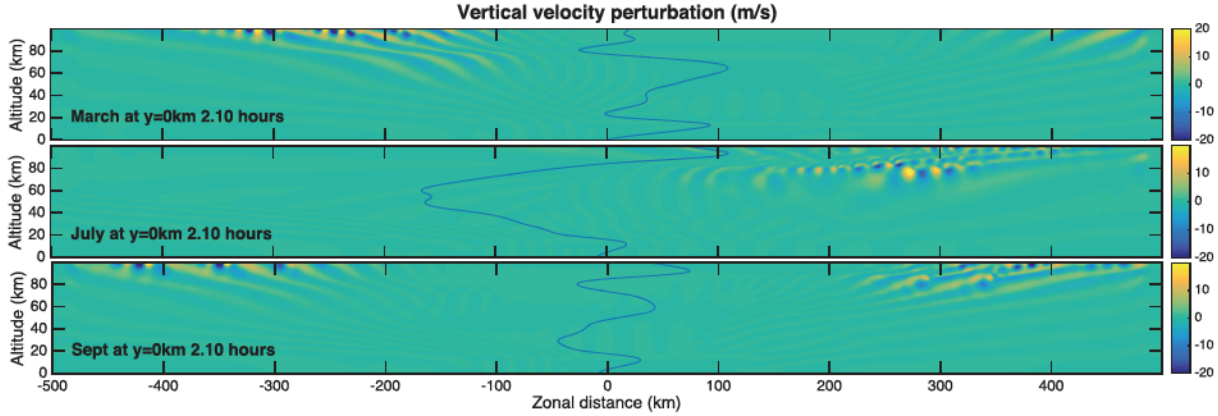

Figure 4. Zonal slice of the vertical velocity perturbation for the March, July, and Sept cases at $t = 2.1$ hr with the native aspect ratio for reference. The blue lines are a representation of the shape of the background wind.

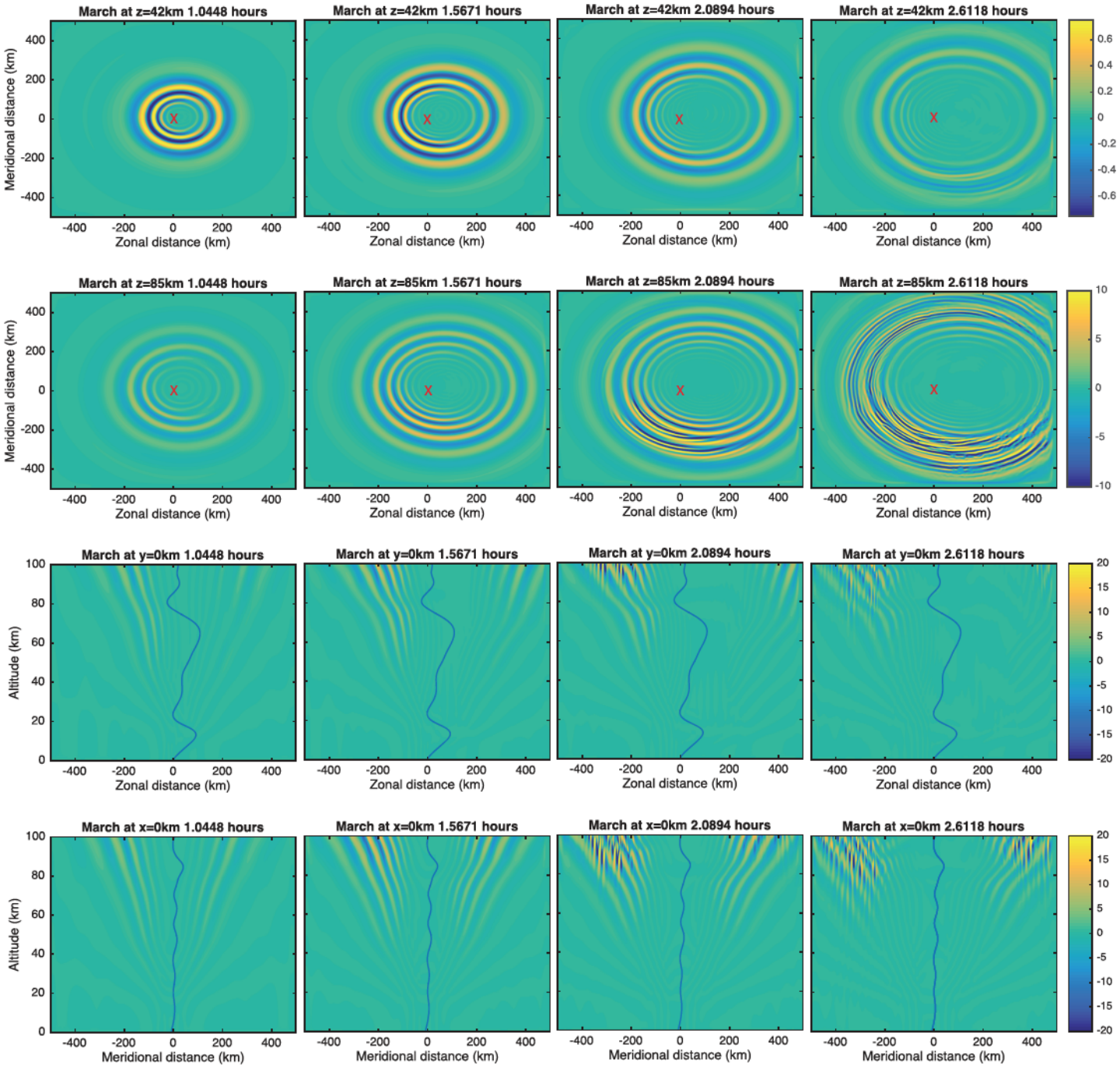

Figure 5. The evolution of a convectively generated gravity wave (w, m/s) through a typical March background atmosphere in the low latitudes. The top row shows the time evolution (from left to right) of the vertical velocity perturbation in the stratosphere (at 42 km). The second row shows the time evolution of the vertical velocity perturbation at 85 km altitude (mesosphere). The third row shows a zonal slice through the domain, with the blue line representative of the background zonal wind (not to scale). The last row shows the time evolution of a meridional slice through the domain, with the blue line representing the meridional wind (not to scale). Red crosses indicate the center of the domain ($x = 0, y = 0$).

larger scales than the primary wave and is driven by packet-scale dissipation (Vadas et al., 2018). Figure 6 show a z-t cross section of Figure 5 at $x = 0$, $y = -350$ and highlights downward propagating waves (and some reflection) originating from a breaking region at z ~110 km and t ~1.75 hr that reach $z = 42$ km at t ~2.3 hr with amplitudes of ~0.5 m/s. It is also noted that the apparent center of the concentric ring in Figure 5 shifts eastward over time, as suggested in Vadas et al. (2009). This is a result of faster horizontal group velocities for CGWs propagating eastward (with the wind) as opposed to westward (against the wind).

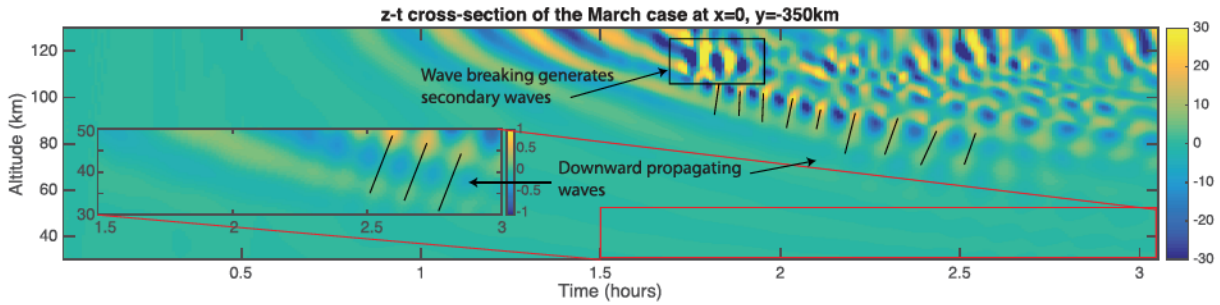

Figure 6. The *z-t* cross section of the vertical wind in the March simulation at $x = 0$, and $y = -350$ km (with different color scales for each altitude region). The plot show downward propagating waves, apparently emanating from a breaking region at ~110 km altitude, that reach 42 km altitude beyond t ~2.3 hr.

In the mesosphere (second row of Figure 5), there is a clear preference for larger amplitudes and initial CGW breaking in the southwestern direction that spreads around the concentric ring by $t = 2.6118$ hr. The CGW breaking forms interference patterns and is generally aligned with the propagation direction of the concentric ring. The shift to a predominant southwesterly direction occurs as a result of the relative weakening zonal winds and strengthened meridional wind at 85 km (wind is north easterly at 85 km).

In the zonal plane (third row of Figure 5) at $y = 0$, there is a clear preference for westward propagation and the eastward propagating components are partially filtered by the predominantly eastward winds. The westward propagating components of the CGW will also have larger vertical group velocities and thus reach higher altitudes before the same spectral component that is propagating eastward. Breaking occurs in the thermosphere around $t = 2$ hr and then proceeds to cascade to lower altitudes. The zonal plane view clearly shows how the westward propagating components are closer to the source location than the eastward propagating components at any given time. This, once again, is due to the differences in horizontal group velocities for waves propagating with and against the wind and leads to the apparent shifting of the center of the concentric ring.

In the meridional plane (bottom row of Figure 5) at $x = 0$, there is far greater symmetry between the westward and eastward propagating CGW components due to the negligible winds in the meridional direction. CGW breaking occurs above 80 km in both the southward and northward directions but is more prominent in the southward direction. This is because the mean meridional wind is northward leading to larger vertical wavelengths for southward propagating CGW. Larger vertical wavelengths lead to enhancements in the vertical wind amplitude. Generally, the meridional wind is predominantly northward from the ground to 87 km; thus, on average, southward propagating CGWs will have larger vertical wavelengths and group velocities and will propagate up to the mesosphere faster than the northward CGWs; therefore, the breaking will likely occur earlier for southward propagating CGWs as a result. Breaking also initiates slightly lower in the atmosphere in the southward direction.

3.1.2. July Evolution

The evolution of the CGW propagating through the July averaged background is shown in Figure 7. At 42 km altitude (top row in Figure 7), the CGW amplitude is strongest in the eastward direction (against the strong westward stratospheric winds). The morphology of the CGW is distinctly arc shaped and a complete concentric ring is not formed. This is consistent with the results of Vadas et al. (2009) in the presence of strong winds. Essentially, the portion of the CGW traveling westward is highly filtered by the prevailing winds and only waves with phase speeds greater that ~50 m/s can propagate into the upper stratosphere and beyond. As time progresses, numerous scales and interference patterns are seen in the portion of the CGW propagating eastward, southeastward, and northeastward. The specific CGW scales seen at a given time result from different CGW modes reaching 42 km at different times along different azimuths. This occurs because of azimuthal differences in wind, which lead to different vertical and horizontal group velocities along each azimuth. The interference pattern is also partially the result of downward propagating waves from breaking in the mesosphere and above. As pointed out in Vadas et al. (2009), some portion of the CGW spectrum propagating against the strong solstice wind will also be reflected leading to gaps in the spectra at certain radii.

In the mesosphere (second row of Figure 7), CGW breaking occurs within three consecutive wavefronts at $t = 1.5795$ hr in the eastward direction. The CGW breaking then cascades along the concentric wavefronts

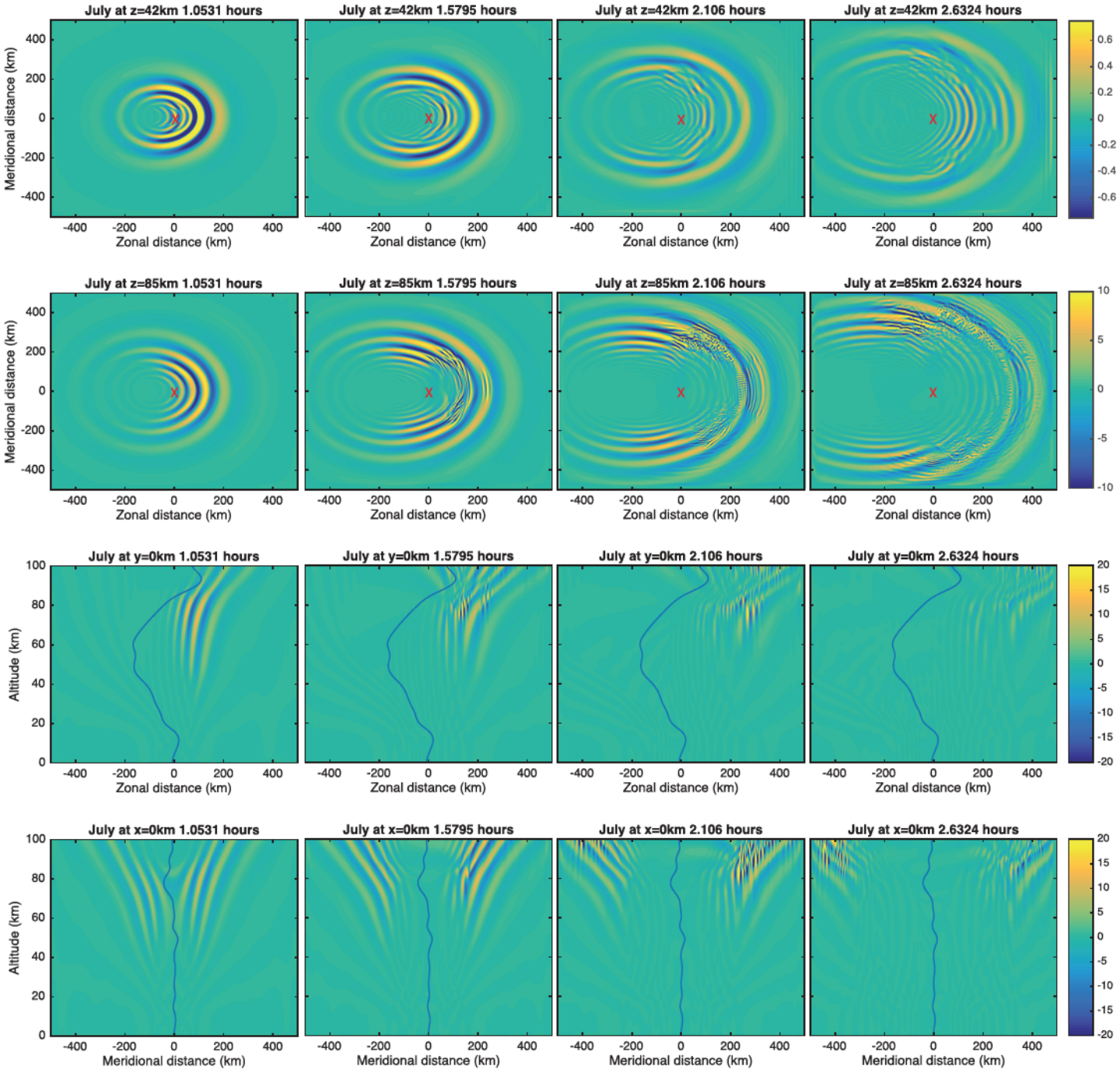

Figure 7. The evolution of a convectively generated gravity wave (w, m/s) through a typical July background atmosphere in the low latitudes. The top row shows the time evolution (from left to right) of the vertical velocity perturbation in the stratosphere (at 42 km). The second row shows the time evolution of the vertical velocity perturbation at 85 km altitude (mesosphere). The third row shows a zonal slice through the domain, with the blue line representative of the background zonal wind (not to scale). The last row shows the time evolution of a meridional slice through the domain, with the blue line representing the meridional wind (not to scale). Red crosses indicate the center of the domain ($x = 0, y = 0$).

from the zonal to the meridional direction as time progresses, with the strongest breaking occurring in the northeastern direction. The CGW breaking is initiated by the strong shear in the zonal wind (as can be seen in the third row of Figure 7) and is initially aligned with the concentric wavefront but evolves into a structure

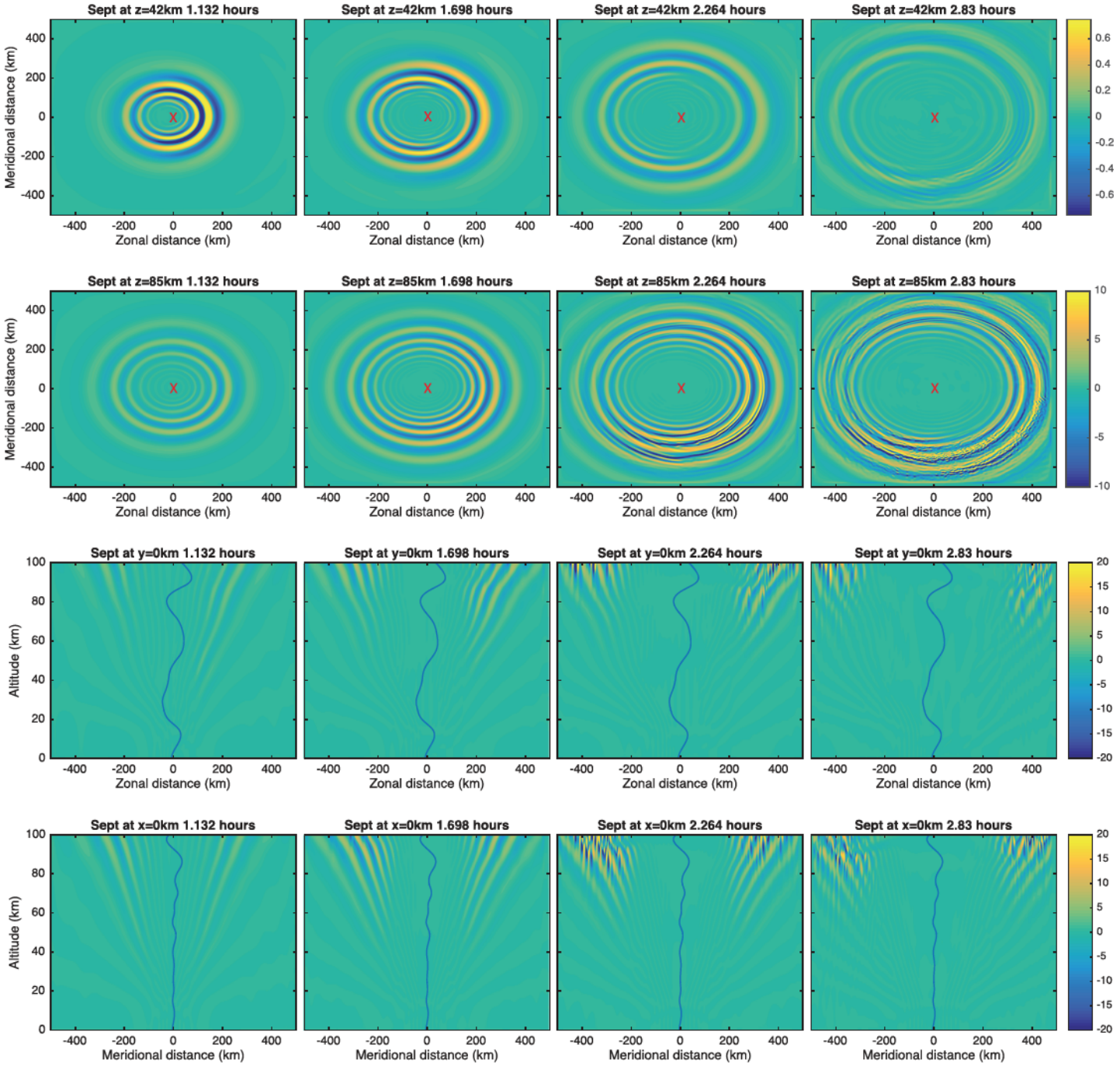

Figure 8. The evolution of a convectively generated gravity wave (w, m/s) through a typical September background atmosphere in the low latitudes. The top row shows the time evolution (from left to right) of the vertical velocity perturbation in the stratosphere (at 42 km). The second row shows the time evolution of the vertical velocity perturbation at 85 km altitude (mesosphere). The third row shows a zonal slice through the domain, with the blue line representative of the background zonal wind (not to scale). The last row shows the time evolution of a meridional slice through the domain, with the blue line representing the meridional wind (not to scale). Red crosses indicate the center of the domain ($x = 0, y = 0$).

that is perpendicular to the concentric wavefront. This is in contrast to the breaking seen in March, which remains aligned with the concentric wavefront.

In the zonal cross section (third row of Figure 7), almost all of the CGW visible is propagating in the eastward direction. Breaking initiates around 80 km altitude (much lower than in March) due to the local wind shear and creates secondary waves that propagate upward and downward and in both east and westward directions. The breaking then decays and dissipates as time progresses.

In the meridional cross section (bottom row of Figure 7), the CGWs initially propagates symmetrically in the north and south directions. By $t = 1.5795$ hr, breaking is initiated in the northward propagating CGW at ~80 km altitude. As time progresses, breaking is present in both the north and southward directions but with different characteristics, evolution, and altitudes.

3.1.3. September Evolution

In the stratosphere (top row in Figure 8), the largest w amplitude (1.6 m/s) portion of the wave packet propagates eastward and occurs 1.132 hr into the simulation. At this altitude, the zonal wind is westward causing the eastward propagating components to have larger vertical wavelengths and vertical group velocities (and hence larger w amplitudes). As time progresses, the dominant propagation direction shifts toward the meridional with similar amplitudes in both the north and southward directions. This rotation of the dominant propagation direction from eastward toward the north and south occurs because of the change in vertical group velocity with azimuth. CGW modes propagating eastward have larger vertical group velocities (for the same horizontal wavelength and period) and reach the stratosphere first, while the north and southward components have smaller vertical group velocities and reach the stratosphere later. At 2.8 hr, small horizontal scales appear within the larger horizontal scales and cause interference patterns in the CGW morphology. The amplitudes of these waves are small (0.2–0.3 m/s vertical velocity) and result from downward propagating waves that come from the breaking region in the upper atmosphere (similarly to the March case). The CGW pattern, due to the small winds in the September case, is the most concentric of all the three cases.

In the mesosphere (85 km), the dominant CGW propagation direction is toward the southeast and reaches an amplitude of 9 m/s vertical velocity (at 1.7238 hr) before the CGW breaks into smaller structure and the vertical velocity increases to between 30 and 40 m/s vertical velocity. The breaking initiates in the trough of the CGW (minimum vertical velocity perturbation) and then evolves to smaller scales which are mostly aligned with the phase of the CGW.

In the zonal plane ($y = 0$), the eastward tropopause winds tend to filter some of the eastward propagating winds at the source level. The winds in the stratosphere are predominately westward are thus the eastward propagating CGWs have larger w amplitude, larger vertical scales and faster vertical group speeds. In the mesosphere, the wind oscillates between eastward, westward, and eastward again leading to local filtering and refraction of the CGWs. Breaking occurs in the thermosphere after 1.7735 hr, and at different altitudes (and scales) for the east and westward propagating CGWs. For eastward propagating CGWs, breaking occurs between 100 and 130 km altitude, while the westward CGWs break as a result of the westward shear between 100 and 120 km. As time progresses, the breaking progresses downward into the mesosphere but does not descend as low as the breaking in the meridional direction.

In the meridional plane (at $x = 0$), the winds only become appreciable above 80 km altitude. As a result, the northward and southward propagating CGWs are almost identical in this region. Nonlinearity becomes apparent after 1.3962 hr above 100 m altitude. Strong breaking occurs around 1.7452 hr at 105–115 km altitude, with the southward propagating CGWs breaking 5–10 km higher than those propagating northward due to the local shears in the meridional wind. As time progresses, the breaking occurs lower down in the atmosphere.

3.2. CGW Spectra and Filtering

In this section, 2-D Fourier transforms are taken of the zonal-temporal and meridional-temporal domain slices at altitudes of 20, 42, and 85 km through the middle of the domain. The zonal-temporal and meridional-temporal slices cover the whole horizontal domain and time period of the simulation. The arrays are windowed using a symmetric hanning window before the 2-D Fourier transform is applied to avoid spectral leakage. This allows us to assess the spectrum at three different layers of the atmosphere and the effects of the winds in filtering the spectrum between those layers. The 2-D fast fourier transform (FFT) of the vertical velocity perturbation is shown in each case and lines are overlaid on the plots to show constant horizontal phase speeds.

At 20 km, in the zonal direction for the March case (top left of Figure 9), it is clear that the spectrum in the lower stratosphere is highly asymmetric. The dominant zonal wavelength and period for the westward propagating CGWs is 61.5 km and 11.93 min, respectively, and the spectrum lies along the 90 m/s phase speed line. In contrast, the eastward propagating CGWs have much slower phase speeds of ~36 m/s. The key driver of this asymmetry is the strong zonal wind and shear in the troposphere which reaches a peak eastward velocity of ~30 m/s at the tropopause. Vadas et al. (2009) explains the asymmetry as a result of

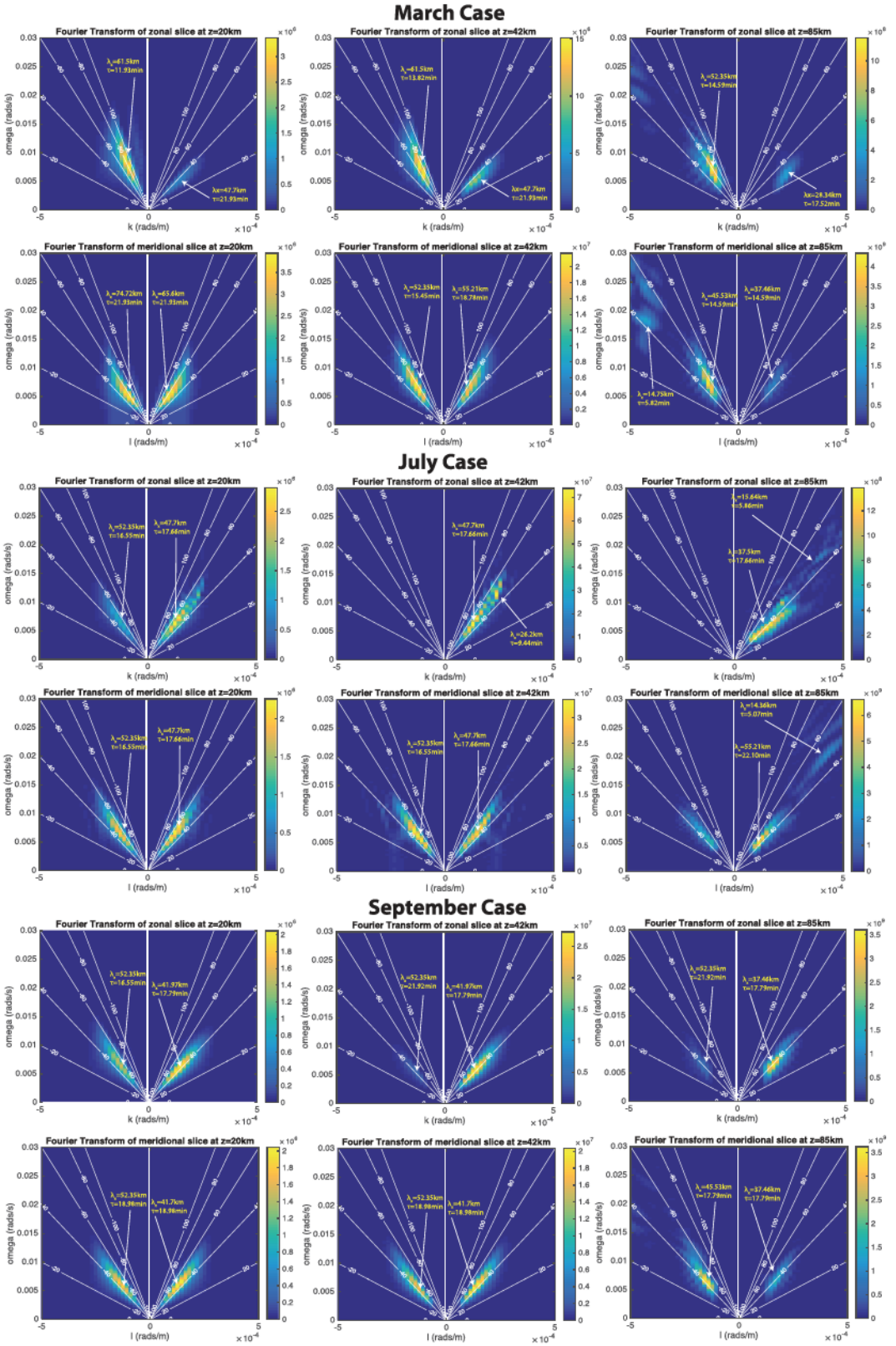

Figure 9. The 2-D Fourier transform for a zonal-temporal slice at $z = 20$ km (left), 42 km (middle), and 85 km (right) and meridional-temporal slice at $z = 20$ km (left), 42 km (middle), and 85 km (right) in the March (first and second rows), July (third and fourth rows), and September case (fifth and sixth rows), respectively. White lines indicate lines of constant horizontal phase speed.

Doppler shifting by the tropopause wind. Essentially, CGWs generated in both directions with the same k are symmetric in the frame of reference of the tropopause wind but are asymmetric in the extrinsic (or ground relative frame). Beres et al. (2002) suggests that the upper tropospheric shear acts similarly to a critical level and reduces the momentum flux of CGWs propagating in the same direction as the storm relative mean wind and enhances the CGWs propagating opposite to the storm relative mean wind. This is certainly the case in the March simulation results, which shows enhancement for westward propagation (opposite the tropospheric wind direction). The difference in the phase speeds of the westward and eastward propagating CGWs is $90 - 36.25 = 53.75$ m/s.

In the July, zonal direction (third row, left panel of Figure 9), the tropopause shear is much smaller than in March and the spectral characteristics at $z = 20$ km are fairly symmetric for the east and westward propagating components. However, the spectral amplitude is much larger for the eastward propagating CGW components as the zonal winds at 20 km altitude are already 20 m/s to the west, which contributes to the amplitude anisotropy.

In the September, zonal direction, at 20 km altitude (fifth row, left panel of Figure 9), the spectral strength is larger for the eastward CGWs although there is still a significant amount of CGW energy propagating westward. The dominant phase speed is faster in the westward than the eastward direction (52.72 and 39.32 m/s, respectively). The dominant wave characteristics for the westward propagating CGWs are the same as the July case, but the eastward propagating CGWs have slightly shorter wavelengths than their July counterparts. In the meridional slice at $z = 20$ km, (left panel, Rows 2, 4, and 6 for March, July, and Sept, respectively), the spectrum remains relatively symmetrical in each case due to the lack of strong meridional wind or shear at $z = 20$ km. Note that the spectra at $z = 20$ km are consistent with previous numerical studies which suggest scales associated with single cloud systems of 5–50 km and 10–60 min periods (Lane & Moncrieff, 2008). They are also consistent with the observed wavelengths in Perwitasari et al. (2016), who found wavelengths of 40–100 km in the mesosphere.

At $z = 42$ km, the spectra remain fairly similar to the spectra at $z = 20$ km in most cases. The only differences arise in July and September, where the westward propagating portions of the CGW have been filtered by the zonal winds and are significantly weaker in amplitude than the eastward propagating components.

In the mesosphere at $z = 85$ km, wave breaking (in situ or otherwise) significantly affects the spectra in each case. In the March mesosphere (top right and second row right column of Figure 9), the dominant phase speed of the westward propagating CGWs is now only ~60 m/s (90 m/s previously) and the eastward propagating CGWs are only ~27 m/s (previously 36 m/s). The parts of the spectrum with smaller k (larger horizontal wavelength), and ω (longer period) that are present in the lower atmosphere are also not present in the mesosphere. This can simply be the result of those components having shallower propagation angles that do not reach the mesosphere over the course of the 3 hr simulation or propagate out of the simulation domain. There is also some spectral power at large ω and k in the westward and southward directions resulting from CGW breaking in the mesosphere. In July, the zonal spectrum predominately aligns itself with the 40 m/s phase speed line (see third row, right panel of Figure 9). The dominant period remains the same as in the lower atmosphere, but the horizontal wavelength is ~10 km smaller in the mesosphere than it is in the stratosphere. This is indicative of the transition to smaller scales associated with the CGW breaking process. There are also much shorter period modes that appear, the most dominant of which has a horizontal wavelength of 15.64 km and a 5.86 min period (phase speed of 44.48 m/s). In September (fifth and sixth rows, right column of Figure 9) the dominant spectral characteristics remain unchanged from those at 42 km altitude. However, the spectrum becomes truncated at small k and ω in both the east and west directions. There is also no strong evidence of wave breaking in the zonal spectrum at 85 km since the breaking initiates higher in the atmosphere (as can be seen in Figure 8) and does not have much influence of the spectra at 85 km altitude.

3.3. Initiation of CGW Breaking

In this section, we examine the altitudes, location, amplitudes, and scales of the onset of breaking in the zonal and meridional planes for each of the three cases. We examine the onset visually from the simulations and compare this with the Richardson number. The Richardson number is defined as $Ri = \frac{N^2}{(\partial u/\partial z)^2}$, where N is the buoyancy frequency and $\partial u/\partial z$ is the vertical shear in the horizontal wind (the zonal wind for the zonal slices and the meridional wind for the meridional slices and includes both background winds and CGW perturbations). It is generally assumed that a flow is shear unstable for $Ri < 0.25$ and convectively

unstable for $Ri < 0$; however, this is also known to be an oversimplification for gravity waves in the atmosphere (Achatz, 2007; Fritts et al., 2009). Figure 10 shows the perturbation velocity and a Ri number logical (1 if Ri<0.25, 0 otherwise), in the zonal plane, at the time of onset of visual breaking. The top panels for each month show the onset of breaking for the westward propagating CGWs, and the bottom panel for the eastward propagating CGWs. The only exception is July, which only has eastward breaking. The blue line and red lines overlaid on the figure represent the background zonal wind (multiplied by 3) and buoyancy frequency squared (multiplied by 3e5) for comparison purposes.

3.3.1. Zonal Breaking

The March westward propagating CGWs show visual breaking at $t = 1.7586$ hr at an altitude range between 110 and 120 km (top left of Figure 10). The Ri plot (top right of Figure 10) shows that the CGW is unstable aligned along specific phase fronts. The breaking is initiated at the stability peak (signified by the red line) caused by the rapidly increasing background temperature in the lower thermosphere. This, combined with a small zonal wind in the westward direction, leads the westward CGWs to refract to small vertical wavelengths. The small vertical wavelength leads to large local shears and temperature gradients causing instability in this region. The breaking is initiated along phase fronts where the local shear is maximized and the temperature gradient is decreasing most rapidly. Note that the Ri number indicated instability about 20 min before visual breaking arises in the simulation. Since the winds are relatively small in the March case, the temperature gradient arising from the transition to the thermosphere is the most significant change in the atmosphere environment that the CGWs encounter at large amplitude, thus breaking does not occur at lower altitudes. At the onset of breaking the peak amplitude of the wind perturbation is −108 m/s and the peak temperature perturbation is 60 K. The vertical spacing between the breaking regions is equal to the vertical wavelength of the CGW (~10 km) and the horizontal scale is ~18 km. The eastward propagating CGWs break later (second row, left column of Figure 10) and at a higher altitude than the westward propagating CGWs (at 2.176 hr and between 120 and 130 km altitude). This is because the zonal wind is opposing the CGW propagation direction between 110 and 120 km, which acts to increase the vertical wavelengths and thus reduce the local shear and temperature gradients in the CGW. Therefore, the CGW can propagate about 10km higher before breaking is initiated, as the wind turns eastward at this altitude. The maximum amplitude of the wind perturbation is 176 m/s and the maximum temperature perturbation is 215 K. The scales of the breaking are larger for the eastward propagating CGWs because of the increased viscosity at the altitude of breaking when compared to the altitude at which the westward CGWs break.

In contrast to the March case, the breaking in the zonal direction in July initiates much lower down at 81 km altitude (third row, left of Figure 10) due to the large zonal wind shear in this region. The breaking also occurs much earlier ($t = 1.3163$ hr vs. $t = 1.7586$ hr) in the July case and corresponds to in situ breaking for the OH layer in particular (which peaks at 87 km). Not only does the large zonal shear create susceptibility to the onset of Kelvin-Helmholtz instability, but the wind is near maximum in the direction of CGW propagation, which minimizes the CGW's vertical wavelength and creates large wind shears and temperature gradients in the perturbation quantities on top of the large mean zonal shear. The Richardson number is negative at 80 km (third row, right column of Figure 10), so both the convective and shear instability conditions are met in this region with the unstable region spanning a depth of one vertical wavelength. The vertical wavelength in the breaking region is 6.5km (compared to 10 km in the March case). The horizontal scales of the breaking are ~15–18 km (similar to the zonal breaking scales in March) compared to a horizontal wavelength of 65 km for the primary CGW. The horizontal perturbation wind amplitudes are ~90 m/s in the breaking region and the perturbation temperature amplitudes are ~45 K. In the fourth row, left panel of Figure 10 at $t = 1.6673$ hr, two further distinct breaking regions are present. The first is at 105 km altitude (corresponding to the stability peak) caused by the same mechanisms as the wave breaking in the March case and with similar scales to the breaking at 80 km altitude. The second region is centered at approximately 135 km altitude and consists of much larger scales than the breaking lower down due to the increased viscosity. One important feature to note is the appearance of westward propagating small-scale secondary waves generated from the wave breaking at 80 km (seen at $x = 100$ km, $z = 105$ km in the fourth row left column of Figure 10). These secondary waves have horizontal wavelengths of ~20 km, which closely correspond to the breaking scales below, and appear to propagate freely up to ~140 km altitude.

For the September eastward propagating CGWs (fifth row, left column of Figure 10), breaking is initiated between 130 and 140 km altitude, the highest of all three cases and which also occurs at the latest time. The breaking scales are large, with horizontal spacing of the breaking structures equal to the horizontal

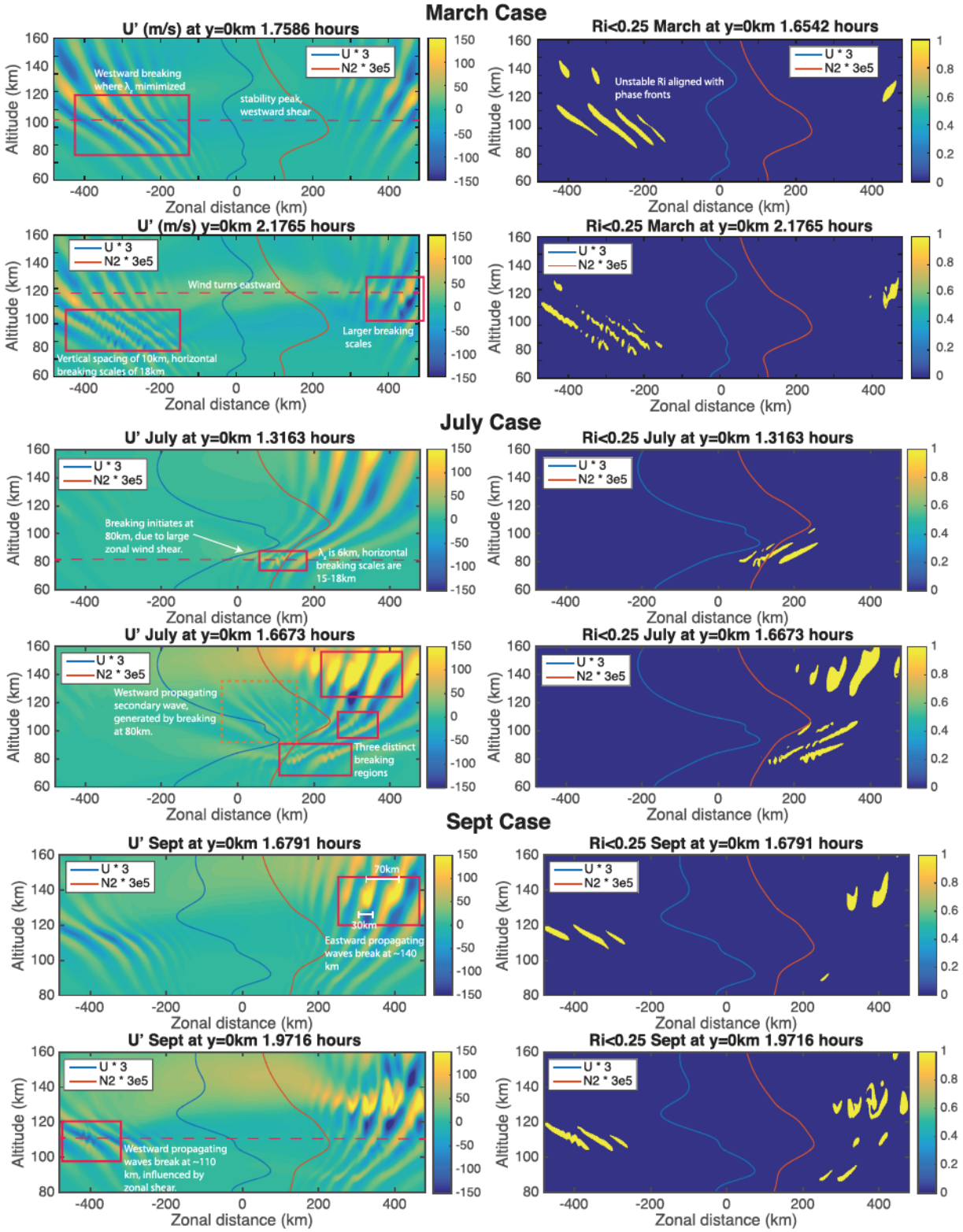

Figure 10. The horizontal perturbation velocity field (left) and a plot of the Richardson number (right) logical (1 if Ri < 0.25, 0 otherwise) at the onset of visible breaking, in the March (top), July (middle), and September (bottom) cases, in the zonal plane. The first, third, and fifth panels show the onset of breaking for westward propagating CGWs (except July, which only has eastward breaking CGWs) and the second, fourth, and sixth panels show the onset of breaking for eastward propagating CGWs. The blue and red lines overlaid represent the zonal wind (multiplied by 3 for ease of viewing) and the buoyancy frequency squared (multiplied by 3e5 for ease of viewing).

wavelength of the CGW (~70 km), with the size of the eddies themselves being around 30 km wide and 10 km deep. The breaking does not appear to be tied to any strong shears in the background zonal wind but results from large shear and temperature gradients associated with the large amplitude of the CGW itself as it grows in amplitude with altitude. The westward propagating CGWs break even later again ($t = 1.9716$ hr) and result from the westward zonal wind shear between 100 and 120 km altitude. The breaking here is specifically shear unstable and the Richardson number barely decreases below 0.25. The horizontal spacing of the instability structures are ~15 km again.

It is already known that the strong zonal winds in the solstice months cause a distortion of the concentric pattern into a squashed arc pattern Vadas et al. (2009), and that strongly filtering occurs for waves propagating with the wind. However, this study shows that strong zonal shears in the mesosphere can create strong in situ breaking for CGW propagating against the stratospheric zonal wind and then in the direction of the mesospheric shear. This can further break up the semiconcentric pattern into smaller turbulent structure in this region, destroying the obvious concentric nature of the CGW seen in the equinox cases and dissipating its energy and momentum. This may further explain why Perwitasari et al. (2016) does not observe many concentric patterns in the mesosphere, in the solstice months but Gong et al. (2015) observed them in the stratosphere, where in situ breaking is not present.

3.3.2. Meridional Breaking

Figure 11 shows the same as Figure 10, but for the meridional plane. The March meridional plane (top row of Figure 11), in some ways, mimics the zonal plane. The southward propagating CGW breaks at the stability peak, influenced by a small southward meridional wind at ~105 km altitude. Once again, this occurs where the vertical wavelength is minimized and the local wave shear and decreasing temperature gradient is maximized. The scales are almost identical to the westward CGWs and the maximum horizontal perturbation of −112 m/s and a maximum temperature perturbation of ~40 K. Visible breaking occurs at $t = 1.6716$ hr for both the southward and northward propagating CGWs, which is in contrast to the east and westward propagating CGWs that break at different times. In the March northward direction, CGW breaking is initiated at two distinct heights, one at ~120 km and the other at ~145 km. The lower region of breaking occurs where the wind turns slightly northward and produces scales with horizontal spacing of ~67 km (equal to the horizontal wavelength) and has an amplitude of ~120 m/s and an 80 K temperature perturbation. The upper level breaking at $z = 145$ km has larger scales again due to the high viscosity in this region which dissipates small scales. The breaking here is the result of convective instability exclusively resulting from large perturbation temperature gradients as opposed to large wind shears.

In July, the meridional winds and shears are far smaller than the zonal shears, thus breaking does not initiate in the mesosphere as it does in the zonal direction. For the northward propagating CGW (second row, left panel) breaking initiates at ~115 km altitude, just above the stability peak in the buoyancy frequency. The southward propagating CGW (third row, left panel) breaks later, higher (~120–125 km) and is influenced by the wind and shear turning southward above 105 km altitude. At $t = 1.9042$ hr, breaking is present from 80 km altitude all the way up to 140 km altitude in the northward propagating direction. The scales of the breaking are similar from 80–110 km altitude (~15 km horizontal spacing), above which the scales increase notably (~28 km horizontal spacing at 140 km altitude) with altitude as molecular viscosity becomes dominant. In the southward direction, the breaking is more confined in altitude by the region of southward wind and shear which helps initiate the breaking in that direction, the horizontal scales of which are ~19 km.

In the September, northward direction (fourth row, left panel), the CGW breaking initiates at 120 km altitude, in the presence of a northward shear and just above the stability peak. The spacing between the breaking forms at scales equal to the horizontal wavelength (~50–80 km) and the eddies themselves are ~22 km wide and 5 km deep. As with the March case, the relatively weak background winds and shears means that breaking initiates at altitudes above the observable airglow layers and cascades downward. Thus, the in situ breaking is not strong enough to majorly disrupt the concentric pattern in the airglow layer and instead appears like superposed smaller scale structure. In the southward direction (fifth row, left), the breaking initiates at two distinct altitudes (110 and 140 km), and two different scales. The breaking at 110km altitude occurs at the stability peak in the N^2 profile and in a region of local southward shear. The vertical wavelength is minimized here (10 km) and the instability scales are small (~15 km horizontally). The breaking at 140 km occurs where the wind is turning southward and the N^2 is declining. The scales are much larger (vertical wavelength of 20 km, vertical eddy scales approximately half the vertical wavelength and horizontal scales of ~22 km) due to the increased wave scales and viscosity in this region.

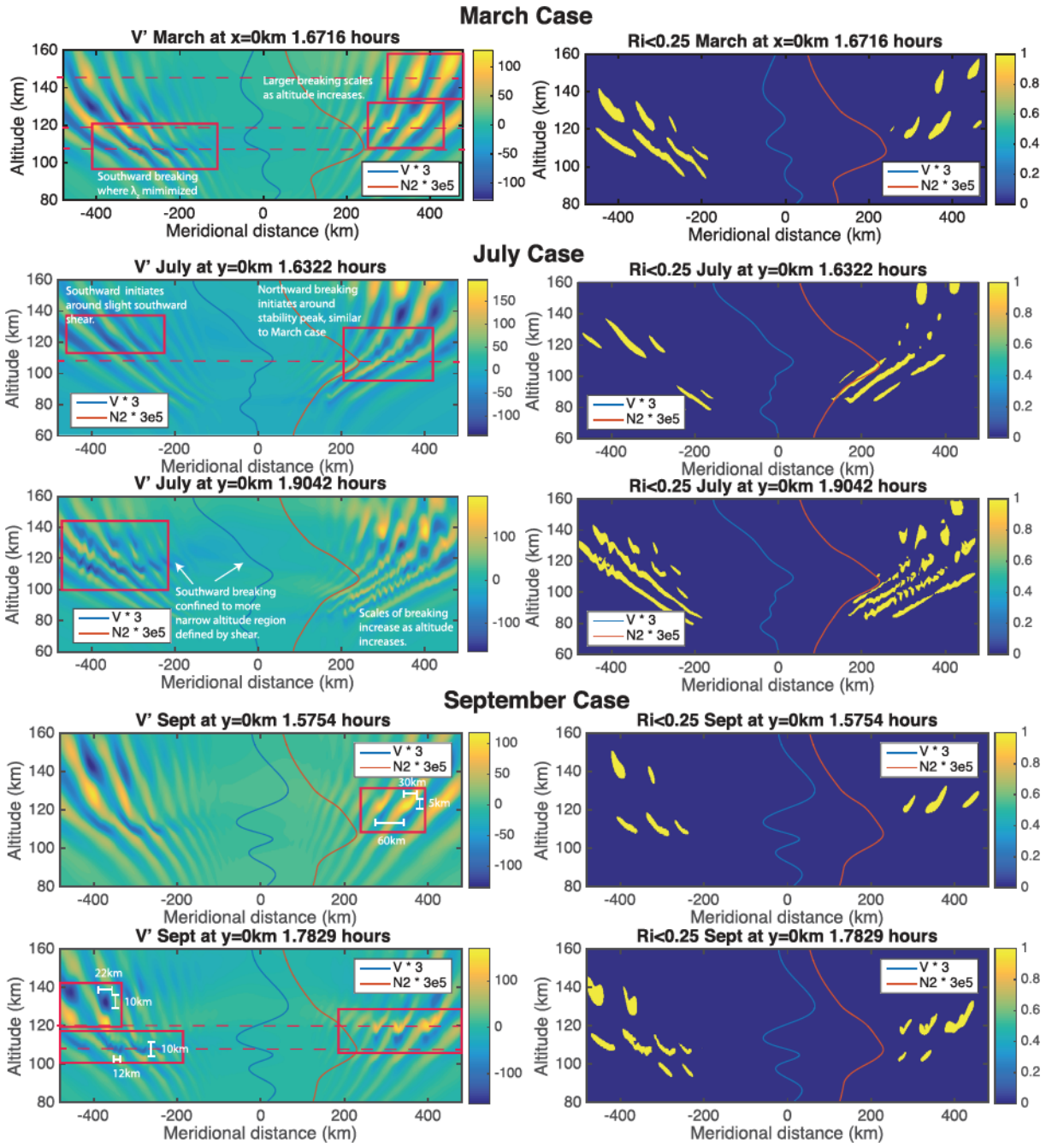

Figure 11. The horizontal perturbation velocity field (left) and a plot of the Richardson number (right) logical (1 if Ri < 0.25, 0 otherwise) at the onset of visible breaking, in the March (top), July (middle), and Sept (bottom) cases, in the meridional plane. The first, second, and fourth panels show the onset of breaking for northward propagating CGWs, and the third and fifth panels show the onset of breaking for southward propagating CGWs. Note that breaking occurs in both the northward and southward directions simultaneously in March. The blue and red lines overlaid represent the zonal wind (multiplied by 3 for ease of viewing) and the buoyancy frequency squared (multiplied by 3e5 for ease of viewing).

In the context of CGW observations in the airglow layers, it is clear the CGW has a preference to break at altitudes above the OH and OI peaks in the equinox cases. Therefore, the concentric patterns are not significantly disrupted or broken up at the OH and OI airglow altitudes by CGW breaking but are superposed with smaller scale structure from the downward propagation of secondary waves from above (i.e., Figure 6). While the intervening winds are still the most important factor in determining the observability of a concentric pattern at a given altitude, the lack of strong in situ breaking also contributes to the observability of the concentric patterns.

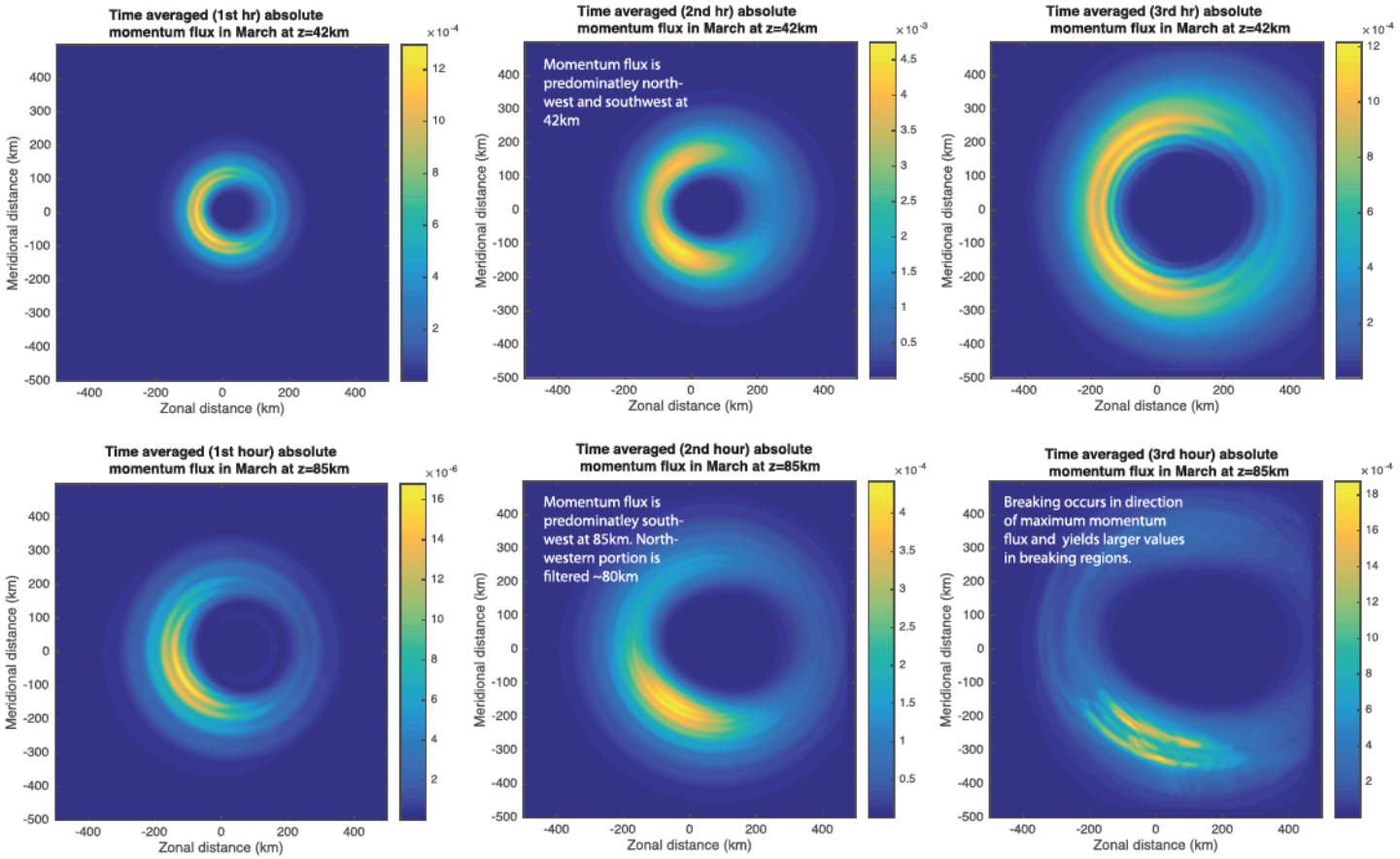

Figure 12. The time-averaged momentum flux at (top) 42 km altitude and (bottom) 85 km altitude for the March simulation. The momentum flux was averaged in 1 hr intervals over (left) the first hour of the simulation, (middle) the second hour of the simulation, (right) the third hour of the simulation.

3.4. Time-Averaged Momentum Flux

In this section, the magnitude of the time-averaged momentum flux ($\overline{\sqrt{(u'w')^2 + (v'w')^2}}$) is investigated at 42 and 85 km (the peak altitudes of the AIRS 4.3 μm emission and OH emission, respectively), for each of the three cases. The momentum flux was averaged over a 1 hr period for the first, second, and third hours of the simulation.

3.4.1. March

Figure 12 shows the time-averaged momentum flux for the March case at $z = 42$ km (top) and 85 km (bottom) over the first (left), second (middle), and third (right) hours of the simulation. At 42 km altitude, the momentum flux consists of expanding rings with a preference toward the western direction during the first hour. In the second hour, the strongest momentum flux values appear in the north and southwest directions, with the southwestern direction having the strongest amplitude. During the third hour, the rings expand and the preferential direction is once again toward the north and southwest but with smaller amplitudes than during the second hour. The calculations show the rotation of the momentum flux over time from the west to the north and southwest. This can occur (1) because of anisotropies in the generated source spectrum as a function of azimuth or (2) due to different vertical propagation times to a given altitude as a function of azimuth. This occurs because the projections of the winds along different azimuths lead to different vertical group velocities (for the same wave mode).

At 85 km (bottom row of Figure 12), the dominant momentum flux is associated with southwestern propagation for all 3 hr of the simulation. The largest momentum values are associated with small-scale structure caused by breaking during the third hour. As seen in Figures 10 and 11, the breaking is initiated lower in both the south and west directions than the north and east directions and then cascades downward. The wind shear in the mesosphere and lower thermosphere as a function of azimuth is large and positive between

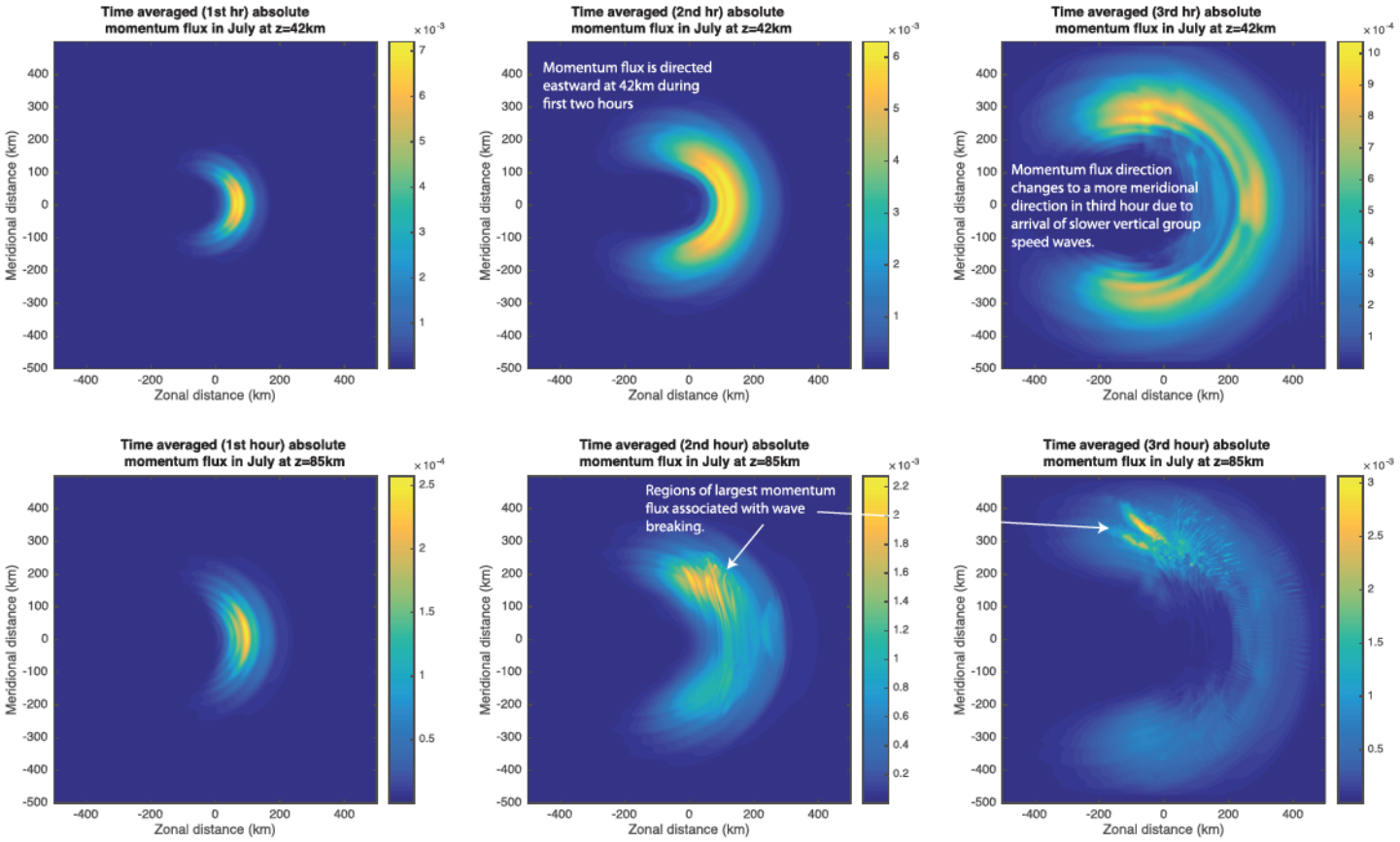

Figure 13. The time-averaged momentum flux at (top) 42 km altitude and (bottom) 85 km altitude for the July simulation. The momentum flux was averaged in 1 hr intervals over (left) the first hour of the simulation, (middle) the second hour of the simulation, (right) the third hour of the simulation.

159° and 233° and is maximized at 192° from north at 110 km altitude. This corresponds with the height and azimuth at which breaking initiates and thus the momentum flux is dominant along this azimuth.

3.4.2. July

Figure 13 shows the same as Figure 12 but for the July simulation. At $z = 42$ km, the momentum flux is entirely to the east due to strong filtering of the westward propagating CGWs by the stratospheric winds. In the third hour, the momentum flux shows three distinct directions of strong momentum flux: north, east, and south. However, the amplitudes are far less than during the first 2 hr. The prominent directions are the result of the meridional components having much slower vertical group velocities than the eastward component and thus reaching the stratosphere at later times. There is also the influence of reflected wave components in the eastward direction and downward propagating secondary waves from breaking in the upper regions of the atmosphere.

At $z = 85$ km, the momentum flux is dominated by the in situ breaking caused by the large zonal wind shear in the mesosphere. The breaking is strongest in the northern flank of the semiconcentric arc and moves from a more zonal propagation direction (in the second hour), to a northeastern direction in the third hour. As can be seen in the second row of Figure 7, the breaking initiates in the zonal direction and then cascades around the arc of the concentric pattern in both the north and south directions, but is strongest in the northern direction. This occurs because the wind shear is strong between 35° and 152° of azimuth (from north) at 85 km altitude but quickly decays between 152° and 180° azimuth. It is also noted that the momentum flux associated with the in situ breaking in July is much larger than any breaking in March or September.

3.4.3. September

Figure 14 shows the time-averaged momentum flux in the September case. At $z = 42$ km, the momentum flux distribution looks similar to that in June but with a more complete concentric shape due to weaker winds and shear. The momentum flux is predominantly eastward in Hours 1 and 2, then switch to the meridional direction in the third hour. As with the June case, the momentum flux switches to the meridional direction in

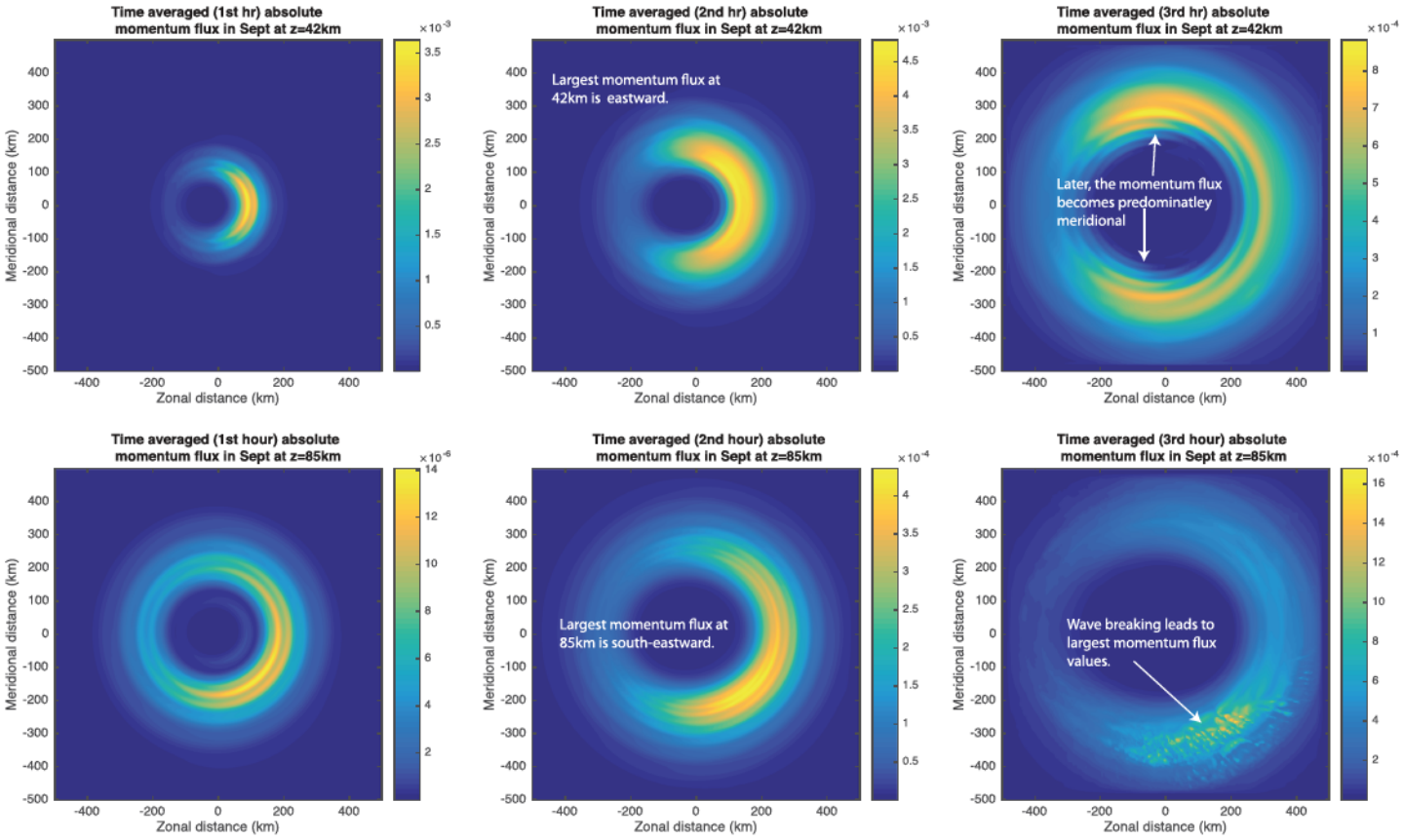

Figure 14. The time-averaged momentum flux at (top) 42 km altitude and (bottom) 85 km altitude for the September simulation. The momentum flux was averaged in 1 hr intervals over (left) the first hour of the simulation, (middle) the second hour of the simulation, (right) the third hour of the simulation.

the third hour because the meridional CGWs have a slower vertical group velocity than the eastward CGWs and arrive later. The winds are smaller in the meridional direction and thus those CGWs are not affected much by the wind refraction, which partially controls the vertical group velocity.

In the mesosphere at 85 km, the momentum flux is concentrated along the southeastern propagation direction, with the largest amplitudes relating to small scales arising from CGW breaking. The shear at 110 km altitude (where the breaking initiates) is maximized along 180° from north and at 85 km altitude it is maximized at an azimuth of 100° from north. It is thus unclear why the momentum flux has a preference for an angle of ~150° azimuth

In general, the momentum flux tends rotate from a preferred zonal direction to a meridional direction, over time, in the stratosphere. In the mesosphere, the preferred direction depends mostly upon the maxima in wind direction and shear with the CGW breaking and small-scale structure yielding the largest momentum flux values.

4. Summary and Conclusions

In the paper, 3-D simulations of CGW propagation were performed under equinox (March and September), and solstice (July) monthly averaged conditions. The aim of which was to explore possible reasons why concentric patterns were more readily observed in equinox months than solstice months in the mesosphere (Perwitasari et al., 2016). The advancement of this work over Vadas et al. (2009) is the inclusion of nonlinearity, wave breaking and secondary wave generation. The effect of these nonlinear features on the morphology and evolution of the concentric patterns are considered, as well as the conditions that lead to wave breaking.

It is well known that the winds are far weaker around the equinox months than they are in the solstice months and that winds play a significant role in the refraction, reflection, filtering, and breaking of CGWs.

Vadas et al. (2009) showed that the most complete concentric pattern would be expected in March (due to small winds and shears) and the most arc-like shape in July (due to largest shear and winds) and the generated spectrum will be most asymmetric in March due to the relatively strong tropopause wind. As with Vadas et al. (2009), this paper finds that intervening weak winds and shears in the equinox months lead to more complete concentric rings in the mesosphere because of the lack of CGW filtering and the relatively constant vertical group velocity as a function of azimuth. The strong winds present in the solstice months lead to arc-like patterns resulting from strong zonal CGW filtering in the stratosphere and the relatively large change in wind with azimuth. It is also noted that the March conditions had a much larger tropopause wind and shear, when compared to the other months, which is known to have a strong influence on the source spectrum (Beres et al., 2002, 2004). This anisotropy in the source was evident in the simulation performed here.

Nonlinearity and CGW breaking can also strongly influence the morphology of a concentric pattern in the mesosphere. In the July case (solstice), breaking initiates in situ at ~85 km altitude as a result of the strong zonal shears in this region. The breaking then cascades around the arc from the zonal to the meridional directions as time progresses. The already arc-like pattern is strongly disrupted by the breaking in the eastward direction and the meridionally propagating CGWs become dominant. Therefore, the amplitudes of the CGW in the zonal direction of propagation are dramatically reduced by stratospheric critical level filtering for westward propagation and in situ breaking in the eastward direction. This could explain why concentric patterns are less likely to be observed in the mesosphere during solstice months. It is also key to note that the simulations presented here assume the same source for all three months. In reality, it is likely that the convective sources in July would be much stronger than those in the equinox months and may lead to more severe breaking than seen in these simulations. Hence, they may lead to even more disruption to concentric patterns. In weak winds and shears in the equinox months, the primary CGWs can propagate up to the thermosphere before breaking is initiated (typically between 110 and 140 km altitude) and then the breaking cascades downward. The breaking was particularly influenced by the stability peak at 110 km altitude, which, in conjunction with the local wind shear, refracts the CGW to small vertical wavelengths and induces CGW breaking through large internal wave shears and temperature gradients. The exact height of the initial breaking depends upon the direction of the wind and shear. Typical scales of the breaking were 12–22 km horizontally and 2.5–10 km vertical, with the scales increasing as the altitude of breaking increased (due to increased viscosity damping smaller scales at increasing altitudes). Since the breaking occurs above the mesosphere, it does not significantly disrupt the visible concentric pattern at 85 km altitude. Rather, small-scale structure is superimposed upon the concentric rings either from downward propagating waves generated in the breaking above, or by breaking that has cascaded down from the thermosphere. This suggests the concentric pattern would be easily observable in the mesosphere during equinox months.

The dominant momentum flux direction (time averaged) is westward in March and eastward in July and September at 42 km altitude. These are the propagation directions that oppose the mean stratospheric wind. At 85 km altitude, the dominant propagation directions are SW, NE, and SE for March, July, and September respectively. These directions are heavily influenced by the azimuth of the dominant wind shear and the largest momentum flux amplitudes are associated with small-scale structure and breaking.

The effect of the winds on the morphology of the concentric pattern, along with the role those winds play in generating CGW breaking, has a significant effect on the observability of concentric wave patterns. Gong et al. (2015) describes observing concentric patterns in the stratosphere in July. However, Perwitasari et al. (2016) did not see many concentric patterns in the mesosphere in July when compared to the equinox months. While an arc-like morphology is present in both the stratosphere and the mesosphere in the July simulations, since it is the stratospheric wind that controls the westward CGW filtering, breaking is not present in the stratosphere but is present in the mesosphere. This breaking causes the eastward propagating portion of the CGW to rapidly dissipate and reduce in amplitude. The breaking also cascades along the CGW front in the north and south directions, leaving only the meridional portions of the CGW intact, significantly disrupting the concentric pattern and its observability in the mesosphere. Wave nonlinearity and breaking, which is strong in the mesosphere due to large CGW amplitudes and zonal shears but not in the stratosphere, could explain the difference in observability in the two altitude regions.

Acknowledgments
Research by C. J. Heale, D. C. Fritts, and T. S. Lund were supported under AFOSR MURI (FA9550-18-1-0009) and NASA 80NSSC18K0007. T. S. Lund was also supported by NSF under NSF AGS-1853000. The simulation outputs required to reproduce the figures in this paper are stored online (https://commons.erau.edu/dm-convectively-generated-gravity-waves/1/). We thank the reviewers for taking the time to provide valuable feedback and help us to improve this manuscript.

References

Achatz, U. (2007). Gravity-wave breaking: Linear and primary nonlinear dynamics. *Advances in Space Research*, *40*, 719–733.

Alexander, M. J., & Holton, J. R. (1997). A model study of zonal forcing in the equatorial stratosphere by convectively induced gravity waves. *Journal of the Atmospheric Sciences*, *54*, 408–419. https://doi.org/10.1175/1520-0469(1997)054<0408:AMSOZF>2.0.CO;2

Alexander, M. J., & Holton, J. R. (2004). On the spectrum of vertically propagating gravity waves generated by a transient heat source. *Atmospheric Chemistry and Physics*, *4*, 923–932. https://doi.org/10.5194/acp-4-923-2004

Alexander, M. J., & Rosenlof, K. H. (2003). Gravity-wave forcing in the stratosphere: Observational constraints from the Upper Atmosphere Research Satellite and implications for parameterization in global models. *Journal of Geophysical Research*, *108*(D19), 459. https://doi.org/10.1029/2003JD003373

Azeem, I., Yue, J., Hoffmann, L., Miller, S. D., Straka III, W. C., & Crowley, G. (2015). Multisensor profiling of a concentric gravity wave event propagating from the troposphere to the ionosphere. *Geophysical Research Letters*, *42*, 7874–7880. https://doi.org/10.1002/2015GL065903

Beres, J. H. (2004). Gravity wave generation by a three-dimensional thermal forcing. *Journal of the Atmospheric Sciences*, *61*, 1805–1815.

Beres, J. H., Alexander, M. J., & Holton, J. R. (2002). Effects of tropospheric wind shear on the spectrum of convectively generated gravity waves. *Journal of the Atmospheric Sciences*, *59*(11), 1805–1824.

Beres, J. H., Alexander, M. J., & Holton, J. R. (2004). A method of specifying the gravity wave spectrum above convection based on latent heating properties and background wind. *Journal of the Atmospheric Sciences*, *61*(3), 324–337.

Booker, J. R., & Bretherton, F. P. (1967). The critical layer for internal gravity waves in a shear flow. *Journal of Fluid Mechanics*, *27*, 513–539.

Bossert, K., Fritts, D., Pautet, P. D., Williams, B. P., Taylor, M. J., Kaifler, B., et al. (2015). Momentum flux estimates accompanying multiscale gravity waves over Mount Cook, New Zealand, on 13 July 2014 during the DEEPWAVE campaign. *Journal of Geophysical Research: Atmospheres*, *120*, 9323–9337. https://doi.org/10.1002/2015JD023197

Bossert, K., Kruse, C. G., Heale, C. J., Fritts, D. C., Williams, B. P., Snively, J. B., et al. (2017). Secondary gravity wave generation over New Zealand during the DEEPWAVE campaign. *Journal of Geophysical Research: Atmospheres*, *122*, 7834–7850. https://doi.org/10.1002/2016JD026079

Burleigh, M. R., Heale, C. J., Zettergren, M. D., & Snively, J. B. (2018). Modulation of low-altitude ionospheric upflow by linear and nonlinear atmospheric gravity waves. *Journal of Geophysical Research: Space Physics*, *123*, 7650–7667. https://doi.org/10.1029/2018JA025721

Choi, H. J., & Chun, H. Y. (2011). Momentum flux spectrum of convective gravity waves. Part I: An update of a parameterization using mesoscale simulations. *Journal of the Atmospheric Sciences*, *68*(4), 739–759. https://doi.org/10.1175/2010JAS3552.1

Chun, H. Y., & Kim, Y. H. (2008). Secondary waves generated by breaking of convective gravity waves in the mesosphere and their influence in the wave momentum flux. *Journal of Geophysical Research*, *113*, D2310. https://doi.org/10.1029/2008JD009792

Drob, D. P., Emmert, J. T., Crowley, G., Picone, J. M., Shepherd, G. G., Skinner, W., et al. (2008). An empirical model of the Earth's horizontal wind fields: HWM07. *Journal of Geophysical Research*, *113*, A12304. https://doi.org/10.1029/2008JA013668

Durran, D., & Klemp, J. (1987). Another look at downslope winds. Part II: Nonlinear amplification beneath wave-overturning layers. *Journal of the Atmospheric Sciences*, *44*, 3402–3412. https://doi.org/10.1175/1520-0469(1987)044<3402:ALADWP>2.0.CO;2

Ern, M., Preusse, P., & Riese, M. (2015). Driving of the SAO by gravity waves as observed from satellite. *Annales Geophysicae*, *33*(4), 483–504. https://doi.org/10.5194/angeo-33-483-2015

Felten, F. N., & Lund, T. S. (2006). Kinetic energy conservation issues associated with the collocated mesh scheme for incompressible flow. *Journal of Computational Physics*, *215*(2), 465–484. https://doi.org/10.1016/j.jcp.2005.11.009

Fovell, R., Durran, D., & Holton, J. R. (1992). Numerical simulations of convectively generated stratospheric gravity waves. *Journal of the Atmospheric Sciences*, *49*, 1427–1442.

Fritts, D., & Alexander, M. J. (2003). Gravity wave dynamics and effects in the middle atmosphere. *Reviews of Geophysics*, *41*(1), 1003. https://doi.org/10.1029/2001RG000106

Fritts, D. C., Wang, L., Werne, J., Lund, T., & Wan, K. (2009). Gravity wave instability and dynamics at high Reynolds numbers. Part I: Wave field evolution at large amplitudes and high frequencies. *Journal of the Atmospheric Sciences*, *66*, 1126–1147.

Garcia, R. R., Dunkerton, T. J., Lieberman, R. S., & Vincent, R. A. (1997). Climatology of the semiannual oscillation of the tropical middle atmosphere. *Journal of Geophysical Research*, *102*(D22), 26,019–26,032. https://doi.org/10.1029/97JD00207

Garcia, R. R., & Solomon, S. (1985). The effect of breaking gravity waves on the dynamics and chemical composition of the mesosphere and lower thermosphere. *Journal of Geophysical Research*, *90*, 3850–3868.

Gong, J., Yue, J., & Wu, D. L. (2015). Global survey of concentric gravity waves in AIRS images and ECMWF analysis. *Journal of Geophysical Research: Atmospheres*, *120*, 2210–2228. https://doi.org/10.1002/2014JD022527

Heale, C. J., Bossert, K., Snively, J. B., Fritts, D. C., Pautet, P. D., & Taylor, M. J. (2017). Numerical modeling of a multiscale gravity wave event and its airglow signatures over Mount Cook, New Zealand, during the DEEPWAVE campaign. *Journal of Geophysical Research: Atmospheres*, *122*, 846–860. https://doi.org/10.1002/2016JD025700

Heale, C. J., Snively, J. B., Hickey, M. P., & Ali, C. J. (2014). Thermospheric dissipation of upward propagating gravity wave packets. *Journal of Geophysical Research: Atmospheres*, *119*, 3857–3872. https://doi.org/10.1002/2013JA019387

Heale, C. J., Walterscheid, R. L., & Snively, J. B. (2018). Localization effects on the dissipation of gravity wave packets in the upper mesosphere and lower thermosphere. *Journal of Geophysical Research: Atmospheres*, *123*, 8915–8935. https://doi.org/10.1029/2017JD027617

Hickey, M. P., Walterscheid, R. L., & Schubert, G. (2011). Gravity wave heating and cooling of the thermosphere: Roles of the sensible heat flux and viscous flux of kinetic energy. *Journal of Geophysical Research*, *116*, A12326. https://doi.org/10.1029/2010JA016792

Hocke, K., & Schlegel, K. (1996). A review of atmospheric gravity waves and travelling ionospheric disturbances: 1982-1995. *Annales Geophysicae*, *14*(9), 917–940. https://doi.org/10.1007/s00585-996-0917-6

Hoffmann, L., & Alexander, M. J. (2010). Occurrence frequency of convective gravity waves during the North American thunderstorm season. *Journal of Geophysical Research*, *115*, D2011. https://doi.org/10.1029/2010JD014401

Holton, J. R. (1982). The role of gravity wave induced drag and diffusion in the momentum budget of the mesosphere. *Journal of the Atmospheric Sciences*, *39*, 791–799.

Holton, J. R. (1983). The influence of gravity wave breaking on the general circulation of the middle atmosphere. *Journal of the Atmospheric Sciences*, *40*, 2497–2507.

Holton, J. R., & Alexander, M. J. (1999). Gravity waves in the mesosphere generated by tropospheric convention. *Tellus B*, *51*(1), 45–58. https://doi.org/10.1034/j.1600-0889.1999.00005.x

Holton, J. R., & Alexander, M. J. (2000). The role of waves in the transport circulation of the middle atmosphere. In G. M. Ser (Ed.), *Atmospheric science across the stratopause* (vol. 123, pp. 21–35).

Horinouchi, T., Nakamura, T., & Kosaka, J. i. (2002). Convectively generated mesoscale gravity waves simulated throughout the middle atmosphere. *Geophysical Research Letters*, *29*(21), 3–1-3-4. https://doi.org/10.1029/2002GL016069

Hunsucker, R. D. (1982). Atmospheric gravity waves generated in the high-latitude ionosphere: A review. *Reviews of Geophysics*, *20*(2), 293–315. https://doi.org/10.1029/RG020i002p00293

Kalisch, S., Chun, H. Y., Ern, M., Preusse, P., Trinh, Q. T., Eckermann, S. D., & Riese, M. (2016). Comparison of simulated and observed convective gravity waves. *Journal of Geophysical Research: Atmospheres*, *121*, 13,474–13,492. https://doi.org/10.1002/2016JD025235

Kirchengast, G., Hocke, K., & Schlegel, K. (1995). Gravity waves determined by modeling of traveling ionospheric disturbances in incoherent-scatter radar measurements. *Radio Science*, *30*(5), 1551–1567. https://doi.org/10.1029/95RS02080

Lane, T. P., & Moncrieff, M. W. (2008). Stratospheric gravity waves generated by multiscale tropical convection. *Journal of the Atmospheric Sciences*, *65*(8), 2598–2614. https://doi.org/10.1175/2007JAS2601.1

Lane, T. P., Reeder, M. J., & Clark, T. L. (2001). Numerical modeling of gravity wave generation by deep tropical convection. *Journal of the Atmospheric Sciences*, *58*, 1249–1274.

Lane, T. P., & Sharman, R. D. (2008). Some influences of background flow conditions on the generation of turbulence due to gravity wave breaking above deep convection. *Journal of Applied Meteorology and Climatology*, *47*(11), 2777–2796. https://doi.org/10.1175/2008JAMC1787.1

Lindzen, R. S. (1981). Turbulence and stress owing gravity wave and tidal breakdown. *Journal of Geophysical Research*, *86*(C10), 9707–9714.

Lund, T. S., & Fritts, D. C. (2012). Numerical simulation of gravity wave breaking in the lower thermosphere. *Journal of Geophysical Research*, *117*, D21105. https://doi.org/10.1029/2012JD017536

Mapes, B. E. (1993). Gregarious tropical convection. *Journal of the Atmospheric Sciences*, *50*(13), 2026–2037.

McFarlane, N. A. (1987). The effect of orographically excited gravitywave drag on the general circulation of the lower stratosphere and troposphere. *Journal of the Atmospheric Sciences*, *44*, 1775–1800.

Miller, S. D., Straka, W. C., Yue, J., Smith, S. M., Alexander, M. J., Hoffmann, L., et al. (2015). Upper atmospheric gravity wave details revealed in nightglow satellite imagery. *Proceedings of the National Academy of Sciences*, *112*(49), E6728–E6735. https://doi.org/10.1073/pnas.1508084112

Nastrom, G. D., & Fritts, D. (1992). Sources of mesoscale variability of gravity waves, Part I, Topographic excitation. *Journal of the Atmospheric Sciences*, *49*, 101–110.

Pandya, R. E., & Alexander, M. J. (1999). Linear stratospheric gravity waves above convective thermal forcing. *Journal of the Atmospheric Sciences*, *56*, 2434–2446.

Perwitasari, S., Sakanoi, T., Nakamura, T., Ejiri, M. K., Tsutsumi, M., Tomikawa, Y., et al. (2016). Three years of concentric gravity wave variability in the mesopause as observed by IMAP/VISI. *Geophysical Research Letters*, *43*, 11,528–11,535. https://doi.org/10.1002/2016GL071511

Pfister, L., Chan, K. R., Bui, T. P., Bowen, S., Legg, M., Gary, B., et al. (1993). Gravity waves generated by a tropical cyclone during the STEP tropical field program: A case study. *Journal of Geophysical Research*, *98*, 8611–8638.

Piani, C., Durran, D., Alexander, M. J., & Holton, J. R. (2000). A numerical study of three-dimensional gravity waves triggered by deep tropical convection and their role in the dynamics of the QBO. *Journal of the Atmospheric Sciences*, *57*, 3689–3702.

Picone, J. M., Hedin, A. E., Drob, D. P., & Aikin, A. (2002). NRL-MSISE-00 empirical model of the atmosphere: Statisical comparisons and scientific issues. *Journal of Geophysical Research*, *107*(A12), SIA 15–1 - SIA 15-16.

Randall, C. E., Carstens, J., France, J. A., Harvey, V. L., Hoffmann, L., Bailey, S. M., et al. (2017). New AIM/CIPS global observations of gravity waves near 50–55 km. *Geophysical Research Letters*, *44*, 7044–7052. https://doi.org/10.1002/2017GL073943

Richter, J. H., Sassi, F., & Garcia, R. R. (2010). Towards a physically based gravity waves source parameterization in a general circulation model. *Journal of the Atmospheric Sciences*, *67*, 136–156. https://doi.org/10.1175/2009/JAS3112.1

Satomura, T., & Sato, K. (1999). Secondary generation of gravity waves associated with the breaking of mountain waves. *Journal of the Atmospheric Sciences*, *56*(22), 3847–3858. https://doi.org/10.1175/1520-0469(1999)056<3847:SGOGWA>2.0.CO;2

Sentman, D., Wescott, E., Picard, R., Winick, J., Stenbaek-Nielsen, H., Dewan, E., et al. (2003). Simultaneous observations of mesospheric gravity waves and sprites generated by a midwestern thunderstorm. *Journal of Atmospheric and Solar-Terrestrial Physics*, *65*, 537–550.

Snively, J. B., & Pasko, V. P. (2008). Excitation of ducted gravity waves in the lower thermosphere by tropospheric sources. *Journal of Geophysical Research*, *113*, A06303. https://doi.org/10.1029/2007JA012693

Song, I., Chun, H. Y., & Lane, T. P. (2003). Generation mechanisms of convectively forced internal gravity waves and their propagation to the stratosphere. *Journal of the Atmospheric Sciences*, *60*, 1960–1980.

Stephan, C., & Alexander, M. J. (2015). Realistic simulations of atmospheric gravity waves over the continental U.S. using precipitation radar data. *Journal of Advances in Modeling Earth Systems*, *7*, 823–835. https://doi.org/10.1002/2014MS000396

Stephan, C., Alexander, M. J., & Richter, J. H. (2016). Characteristics of gravity waves from convection and implications for their parameterization in global circulation models. *Journal of the Atmospheric Sciences*, *73*, 2729–2742. https://doi.org/10.1175/JAS-D-15-0303.1

Suzuki, S., Shiokawa, K., Otsuka, Y., Ogawa, T., Nakamura, K., & Nakamura, T. (2007). A concentric gravity wave structure in the mesospheric airglow images. *Journal of Geophysical Research*, *112*, D02102. https://doi.org/10.1029/2005JD006558

Trinh, Q. T., Kalisch, S., Preusse, P., Ern, M., Chun, H. Y., Eckermann, S. D., et al. (2016). Tuning of a convective gravity wave source scheme based on HIRDLS observations. *Atmospheric Chemistry and Physics*, *16*(11), 7335–7356. https://doi.org/10.5194/acp-16-7335-2016

Tsuda, T., Nishida, M., Rocken, C., & Ware, R. H. (2000). A global morphology of gravity wave activity in the stratosphere revealed by the GPS occultation data (GPS/MET). *Journal of Geophysical Research*, *105*(D6), 7257–7273. https://doi.org/10.1029/1999JD901005

Vadas, S. L. (2007). Horizontal and vertical propagation and dissipation of gravity waves in the thermosphere from lower atmospheric and thermospheric sources. *Journal of Geophysical Research*, *112*, A06305. https://doi.org/10.1029/2006JA011845

Vadas, S. L., & Fritts, D. C. (2005). Thermospheric responses to gravity waves: Influences of increasing viscosity and thermal diffusivity. *Journal of Geophysical Research*, *110*, D15103. https://doi.org/10.1029/2004JD005574

Vadas, S. L., Fritts, D. C., & Alexander, M. J. (2003). Mechanism for the generation of secondary waves in wave breaking regions. *Journal of the Atmospheric Sciences*, *60*, 194–214.

Vadas, S. L., Yue, J., She, C. Y., Stamus, P. A., & Liu, A. Z. (2009). A model study of the effects of winds on concentric rings of gravity waves from a convective plume near Fort Collins on 11 May 2004. *Journal of Geophysical Research*, *114*, D06103. https://doi.org/10.1029/2008JD010753

Vadas, S. L., Zhao, J., Chu, X., & Becker, E. (2018). The excitation of secondary gravity waves from body forces: Theory and observation. *Journal of Geophysical Research: Atmospheres*, *123*, 9296–9325. https://doi.org/10.1029/2017JD027970

Vincent, R. A., Alexander, M. J., Dolman, B. K., MacKinnon, A. D., May, P. T., Kovalam, S., & Reid, I. M. (2013). Gravity wave generation by convection and momentum deposition in the mesosphere?lower thermosphere. *Journal of Geophysical Research: Atmospheres*, *118*, 6233–6245. https://doi.org/10.1002/jgrd.50372

Walterscheid, R., Schubert, G., & Brinkman, D. (2001). Small-scale gravity waves in the upper mesosphere and lower thermosphere generated by deep tropical convection. *Journal of Geophysical Research*, *106*(D23), 31,825–31,832.

Wen, Y., Zhang, Q., Gao, H., Xu, J., & Li, Q. (2018). A case study of the stratospheric and mesospheric concentric gravity waves excited by thunderstorm in northern china. *Atmosphere*, *9*, 489.

Xu, J., Li, Q., Yue, J., Hoffmann, L., Straka III, W. C., Wang, C., et al. (2015). Concentric gravity waves over northern China observed by an airglow imager network and satellites. *Journal of Geophysical Research: Atmospheres*, *120*, 11,058–11,078. https://doi.org/10.1002/2015JD023786

Yue, J., Miller, S. D., Hoffmann, L., & Straka, W. C. (2014). Stratospheric and mesospheric concentric gravity waves over tropical cyclone Mahasen: Joint AIRS and VIIRS satellite observations. *Journal of Atmospheric and Solar-Terrestrial Physics*, 83–90. https://doi.org/10.1016/j.jastp.2014.07.003

Yue, J., Vadas, S. L., She, C. Y., Nakamura, T., Reising, S. C., Liu, H. L., et al. (2009). Concentric gravity waves in the mesosphere generated by deep convective plumes in the lower atmosphere near Fort Collins, Colorado. *Journal of Geophysical Research*, *114*, D06104. https://doi.org/10.1029/2008JD011244

Zhou, X., Holton, J. R., & Mullendore, G. L. (2002). Forcing of secondary waves by breaking of gravity waves in the mesosphere. *Journal of Geophysical Research*, *107*(D7), ACL 3–1-ACL 3-7. https://doi.org/10.1029/2001JD001204